Improved Comprehensive Control of Modular Multilevel Converter under AC/DC Grid Faults and Harmonic Operation Conditions

Jinmu Lai, *Member, IEEE*, Xianggen Yin, *Member, IEEE*, Xin Yin, *Member, IEEE*, Zia Ullah, *Member, IEEE*, Lin Jiang, *Member, IEEE*, and Zhen Wang

***Abstract*—Recent applications of modular multilevel converter (MMC) have posed various problems such as ac/dc grid faults, asymmetric operation conditions, ac grid voltage excessive harmonics, and ac circulating currents, which deteriorate the system's performance and also threaten the safe operation. In this article, an improved comprehensive control architecture of MMC is proposed to maintain a stable voltage control, eliminate harmonics in ac-side and circulating currents, and dc-bus voltage ripple under ac/dc grid faults and harmonic operation conditions. The proposed comprehensive control consists of improved hierarchical voltage control and repetitive controller-based arm current control. The improved hierarchical voltage control, including a novel negative-sequence current injection and dc-circulating current injection-based leg-averaging control and their seamlessly switching handling, enables the MMC to operate under various operating conditions, thereby producing the arm current reference for inner-loop control. The proposed repetitive controller-based arm current control can recognize the control of multifrequency components of arm current without separating positive-, negative- and zero-sequence current components of ac-side currents and circulating currents. Finally, the simulation and experimental studies of the three-phase MMC were carried out in detail, and the findings demonstrate the efficiency and merits of the proposed control method.**

***Index Terms*—Arm current control, comprehensive control, hierarchical voltage control, modular multilevel converter, repetitive controller.**

I. Introduction

MODULAR multilevel converter (MMC) offers various benefits over conventional voltage source converters and is widely used in flexible dc transmission and distribution applications. The major advantages of MMC include independent control of the active and reactive power, high power quality, high modularity, redundant design, and fault ride-through ability. In [1]–[4], the various potential applications of MMC, including high-voltage direct current, power electronic transformer, and flexible ac transmission systems for augmentation of the construction of ac/dc power grid are discussed in detail.

In general, the control objectives of MMC can be characterized as follows:

1) ac-side symmetrical currents control;
2) dc-bus voltage or power control;
3) circulating current suppression;
4) submodule (SM) capacitor voltage balancing control;
5) ac/dc fault ride-through (FRT).

Recently, several innovative research approaches have been proposed for MMC control. Saeedifard and Iravani [5] and Tu *et al.* [6] presented the MMC's control strategy focused on symmetrical current control combined with circulating current suppression controllers. The control method is relatively straightforward under the normal conditions of the grid. However, the consideration of asymmetric operation conditions is a challenging task due to the high complexity. There are two main asymmetric operations include grid voltage asymmetry and asymmetric arm parameters that may appear in the MMC system [7]. The operating characteristics of the MMC system depend on the operational conditions, and there is plenty of difference between asymmetric and normal conditions, which leads to SM capacitor voltage imbalance, ac side current imbalance, increasing in circulating current, and large dc-bus voltage ripple [8]–[10]. All these factors may influence and compromise on the stable operation of the MMC system. The control strategies for MMC discussed in the abovementioned literature independently regulates the ac-side currents and circulating currents, where the positive- and negative-sequence dual *dq*-axis current controllers for ac-side currents, the positive-, negative-, and zero-sequence circulating current suppression controller for the circulating currents are essentially configured to secure SM capacitor voltage. It can be argued that the previous research makes the controller design more complex.

It should be pointed out that the MMC arm currents contain ac-side current, dc-bus current, and a series of undesired ac circulating currents. It is worthy of mentioning that these currents can be controlled jointly, i.e., arm current control method. The arm current control strategies are proposed in [11] and [12], and

Manuscript received July 27, 2020; revised October 20, 2020; accepted November 11, 2020. Date of publication November 25, 2020; date of current version February 5, 2021. This work was supported by the National Natural Science Foundation of China under Grant 51877089. Recommended for publication by Associate Editor S. Le Menec. (*Corresponding author: Jinmu Lai.*)

Jinmu Lai, Xianggen Yin, Zia Ullah, and Zhen Wang are with the State Key Laboratory of Advanced Electromagnetic Engineering and Technology, Huazhong University of Science and Technology, Wuhan 430074, China (e-mail: laijinmu@126.com; xgyin@hust.edu.cn; ziaullah@hust.edu.cn; wangzhen2016@hust.edu.cn).

Xin Yin and Lin Jiang are with the Department of Electrical Engineering and Electronics, University of Liverpool, Liverpool L69 3GJ, U.K. (e-mail: leoxinyin@qq.com; l.jiang@liverpool.ac.uk).

Color versions of one or more of the figures in this article are available at https://doi.org/10.1109/TPEL.2020.3040297.

Digital Object Identifier 10.1109/TPEL.2020.3040297

verified under the symmetrical grid voltage, but the applicability under the asymmetrical grid is not described. Furthermore, a proportional resonance regulator (PR) and proportional integrator (PI)-vector proportional integrator (VPI) based arm current method were proposed in [13] and [14] that aims to control the three current components in the arm current, but it has been shown that the SM capacitor voltage balancing control was not considered in [13] and [14]. An arm current control strategy for MMC with regard to dc-bus voltage, capacitor voltages, and ac-side currents has proposed in [15], the proposed model is applicable for both symmetrical and asymmetric grid voltage; however, the proportional control is adopted in the inner-current loop; despite asymmetry consideration, the presented model is not able to achieve the zero-tracking error of multifrequency components of arm current. In particular, the leg-averaging control based on dc-circulating current injection is only valid when the MMC synthesizes the dc-bus voltage. The proposed method in [15] is not applicable during pole-to-pole short-circuit fault because the dc-circulating current is not able to transfer the power among three legs.

One of the key problems of the MMC application is dealing with dc short-circuit faults. A variety of dc FRT strategies and appropriate typological submodules are proposed for dc FRT of MMC [16]–[20]. In [16] and [17], the dc FRT control was achieved without considering the unbalanced ac grid condition. In [18] and [19], only the overall average capacitor voltage control was provided for dc FRT; the leg-averaging control should be further considered under the unbalanced ac grid condition. The zero-sequence components were not considered in [20]. However, zero-sequence components are unavoidable in the event of asymmetrical faults on the converter side of the transformer or in a transformer-less scheme [21]. Moreover, the existing techniques on the dc FRT controller independently regulate the ac-side currents and circulating currents, and also in dq-frame. It can be argued that considering the asymmetrical ac grid operating condition may escalate control complexity. As described in [22] and [23], another key issue in MMC is the fault detection technique.

Recently, a number of advanced control and various strategies have been proposed for current loop of MMC with high-precision, fast-response, and disturbances suppression, i.e., PR controller[24], repetitive control (RC) [25], deadbeat control [26], model predictive control (MPC) [27], linear-quadratic regulator (LQR) [28], fuzzy logic controller [29], and feedback linearizing control [30]. Due to multifrequency characteristics of arm current, the RC method has been investigated and applied to the MMC system for circulating current suppression. As reported in [25] and [31]–[33], the parallel operation of the PI and RC can suppress even-order circulating harmonics current of MMC. He *et al.* [34], Yang *et al.*[35], and Moranchel *et al.* [36] used the RC cascaded with PI for suppressing the circulating current. However, the presented RC-based control strategies realize the ac-side current control and circulating current suppression control separately. It has been observed that the structure of the dual current control method is more complex, where RC only realizes the even-order circulating current suppression function. It neither realize the zero-tracking error of the periodic ac-side reference signal nor eliminates the odd-order harmonics caused by the grid voltage distortion and dead time effect [37] on the ac-side current.

In summary, it is important to mention that some challenges associated with existing control methods are still needed to be investigated in view of considering the following limitations.

1) A number of researchers studied and proposed different techniques using ac or dc FRT controller by independently regulating the ac-side currents and circulating currents, which may make the controller design more complex.
2) It has been found that the discussion is limited to specific applications, lacking a general structure that provides the flexibility to incorporate both ac and dc FRT capabilities. Rare studies are available in regard to the control objectives of both ac and dc FRT.
3) The inclusion of RC in the MMC only realizes the even-order circulating current suppression function. As far as we know, few works applying the RC to arm current control have been reported in the literature.

In this article, we contribute to overcoming the research limitations discussed previously, by proposing an improved comprehensive control architecture for MMC in order to achieve ac and dc FRT and multifrequency harmonics suppression jointly. The main objectives of the proposed improved comprehensive control are to: 1) obtain ac fault ride-through capability, 2) obtain dc fault ride-through capability and support ac grid as a Static Synchronous Compensator, 3) secure the MMC through the leg and arm voltage balancing control, 4) eliminate both multifrequency harmonics and ac circulating currents. The main contributions and novelties of this article are stated as follows.

1) We utilized the improved outer-loop hierarchical voltage control and inner-loop repetitive controller-based arm current control for the MMC system under the consideration of ac/dc grid faults and harmonic operation conditions. There is no need of current sequence decomposer and separate circulating current controller design in the proposed method.
2) We developed the decoupling mathematical modeling of comprehensive control architecture of the MMC system.
3) We proposed a novel negative sequence current injection (NSCI) based and dc-circulating current injection (DCCI) based leg-averaging control and their seamlessly switching handling, which enables the MMC to realize the stable voltage control under both ac and dc grid fault conditions, thereby generating arm current reference for inner-loop arm current control.
4) Our proposed RC-based arm current control strategy can recognize the control of multifrequency components of arm current without circulating current suppression controller under various operating conditions.

II. MMC Modeling and Characteristics Analysis

A. MMC Modeling

The topological structure of a MMC is shown in Fig. 1, where u_{sa}, u_{sb}, and u_{sc} indicate the three-phase voltages and i_{a}, i_{b}, and i_{c} are the three-phase currents at ac-side of MMC; L, R are

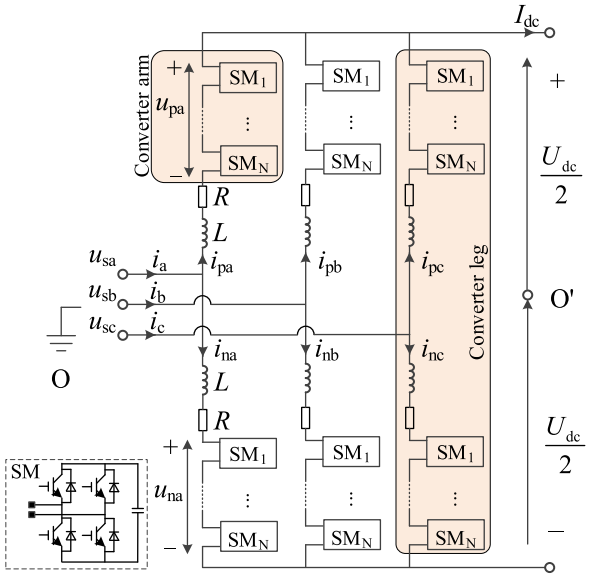

Fig. 1. MMC topological structure.

the arm inductance and equivalent resistance, respectively. The corresponding output voltages for upper arm (p) and lower arm (n) are being represented as u_{pj}, u_{nj} (j = a, b, c), respectively. The upper and lower arms currents are expressed as i_{pj}, i_{nj}. U_{dc} and I_{dc} indicate the dc-bus voltage and current, respectively. $u_{o'o}$ is common mode voltage. Each arm contains N_c SMs. Besides, the reference direction of the variables is shown in Fig. 1.

Applying Kirchhoff voltage law, the voltage equations of j-phase upper and lower arms can be expressed as

$$\begin{cases} u_{pj} = \frac{U_{dc}}{2} + u_{o'o} + L\frac{di_{pj}}{dt} + Ri_{pj} - u_{sj} \\ u_{nj} = \frac{U_{dc}}{2} - u_{o'o} - L\frac{di_{nj}}{dt} - Ri_{nj} + u_{sj}. \end{cases} \tag{1}$$

The relationship among the circulating current, the ac-side current, and the arm current can be written as

$$\begin{cases} i_{pj} = \frac{i_j}{2} + i_{zj} = \frac{i_j}{2} + i_{dcj} + i_{zacj} \\ i_{nj} = \frac{i_j}{2} - i_{zj} = \frac{i_j}{2} - i_{dcj} - i_{zacj} \end{cases} \tag{2}$$

where i_{zj} is the circulating current, i_{dcj} is the dc-component circulating current, and i_{zacj} is a series of undesired ac-component circulating current.

B. Characteristics Analysis under Asymmetry Grid Voltages

In the case of asymmetry grid voltage, to balance the negative- and zero-sequences of the ac grid voltage, the negative- and zero-sequence components in the output voltage of the MMC need to be generated. The output voltage and current of the a-phase leg can be expressed as

$$\begin{cases} e_a = E^+\sin(\omega_1 t + \theta^+) + E^-\sin(-\omega_1 t + \theta^-) \\ \quad\quad + E^0\sin(\omega_1 t + \theta^0) \\ i_a = I^+\sin(\omega_1 t + \varphi^+) + I^-\sin(-\omega_1 t + \varphi^-) \end{cases} \tag{3}$$

where E^+, E^-, $E^0$and θ^+, θ^-, θ^0indicate the positive- negative- and zero-sequence amplitudes and phase angles of MMC output

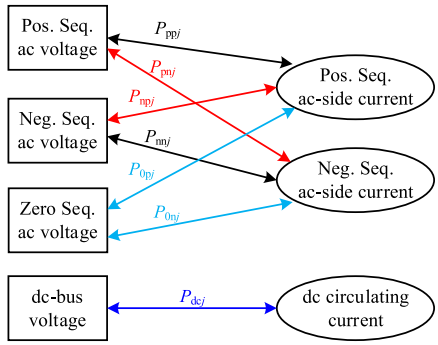

Fig. 2. Definition of the leg average powers caused by positive-, -negative-, zero-sequence voltage and current.

voltage. I^+, I^- and φ^+, φ^- are the positive- and negative-sequence amplitudes and phase angles of the ac-side current, respectively. ω_1 is the fundamental angular frequency.

Assuming that the arm current controller eliminates the ac circulating current in the MMC, i.e., $i_{zacj} = 0$, and considering that the voltage drop of dc-circulating current i_{dcj} on the equivalent resistance R is far less than the dc-bus voltage. Therefore, the instantaneous power of the upper and lower arms, i.e., p_{pj}, p_{nj} of j-phase can be obtained as

$$\begin{cases} p_{pj} = \left(\frac{U_{dc}}{2} - e_j\right)\left(-i_{dcj} - \frac{1}{2}i_j\right) \\ p_{nj} = \left(\frac{U_{dc}}{2} + e_j\right)\left(-i_{dcj} + \frac{1}{2}i_j\right). \end{cases} \tag{4}$$

Then, the average power absorbed by the SM capacitors on the j-leg (j = a, b, c) in one fundamental cycle can be derived as

$$P_j^{\Sigma} = \frac{\omega_1}{2\pi}\int_0^{2\pi/\omega_1}(p_{pj} + p_{nj})\,dt = \frac{\omega_1}{2\pi}\int_0^{2\pi/\omega_1} p_j^{\Sigma} dt. \tag{5}$$

Substituting (3) and (4) into (5), the average power at a, b, c leg can also be expressed as

$$\begin{aligned} 2P_a^{\Sigma} = & -2U_{dc}i_{dca} + E^+I^+\cos(\theta^+ - \varphi^+) \\ & + E^-I^-\cos(\theta^- - \varphi^-) - E^-I^+\cos(\theta^- + \varphi^+) \\ & + E^0I^+\cos(\theta^0 - \varphi^+) - E^+I^-\cos(\theta^+ + \varphi^-) \\ & - E^0I^-\cos(\theta^0 + \varphi^-) \end{aligned} \tag{6}$$

$$\begin{aligned} 2P_b^{\Sigma} = & -2U_{dc}i_{dcb} + E^+I^+\cos(\theta^+ - \varphi^+) \\ & + E^-I^-\cos(\theta^- - \varphi^-) - E^-I^+\cos(\theta^- + \varphi^+ + 120^\circ) \\ & + E^0I^+\cos(\theta^0 - \varphi^+ + 120^\circ) - E^+I^-\cos(\theta^+ + \varphi^- \\ & + 120^\circ) - E^0I^-\cos(\theta^0 + \varphi^- - 120^\circ) \end{aligned} \tag{7}$$

$$\begin{aligned} 2P_c^{\Sigma} = & -2U_{dc}i_{dcc} + E^+I^+\cos(\theta^+ - \varphi^+) \\ & + E^-I^-\cos(\theta^- - \varphi^-) - E^-I^+\cos(\theta^- + \varphi^+ - 120^\circ) \\ & + E^0I^+\cos(\theta^0 - \varphi^+ - 120^\circ) - E^+I^-\cos(\theta^+ + \varphi^- \\ & - 120^\circ) - E^0I^-\cos(\theta^0 + \varphi^- + 120^\circ). \end{aligned} \tag{8}$$

From (6)–(8), the definition of the leg average powers can be illustrated in Fig. 2. During asymmetric grid voltage condition, it can be seen that the average power of the three-phase legs

will no longer be symmetrical. If MMC does not generate a negative-sequence current ($I^- = 0$) or adjust dc-circulating current ($i_{\rm dca} = i_{\rm dcb} = i_{\rm dcc} = i_{\rm dc}/3$), the average power $P_{{\rm np}j}$ and $P_{0{\rm p}j}$ in Fig. 2 are asymmetrical, which will lead to unbalanced SMs capacitor voltages of MMC among three legs. From (6)–(8), a dc-circulating current or ac-side negative-sequence current can be injected instantaneously to average three-phase leg capacitor energies.

1) The average power flow analysis based on dc-circulating current injection.

The average power flow analysis based on dc-circulating current injection was conducted. When MMC takes the three-phase ac-side current symmetry as a control objective, the arm current does not have a negative-sequence current component, i.e., $I^- = 0$. The three-phase average powers without negative-sequence current component can be rewritten as follows:

$$\begin{cases} 2P_a^{\sum} = -2U_{\rm dc}i_{\rm dca} + E^+I^+\cos(\theta^+ - \varphi^+) \\ \qquad -E^-I^+\cos(\theta^- + \varphi^+) + E^0I^+\cos(\theta^0 - \varphi^+) \\ 2P_b^{\sum} = -2U_{\rm dc}i_{\rm dcb} + E^+I^+\cos(\theta^+ - \varphi^+) - E^-I^+\cos(\theta^- \\ \qquad +\varphi^+ + 120^\circ) + E^0I^+\cos(\theta^0 - \varphi^+ + 120^\circ) \\ 2P_c^{\sum} = -2U_{\rm dc}i_{\rm dcc} + E^+I^+\cos(\theta^+ - \varphi^+) - E^-I^+\cos(\theta^- \\ \qquad +\varphi^+ - 120^\circ) + E^0I^+\cos(\theta^0 - \varphi^+ - 120^\circ). \end{cases} \tag{9}$$

The average power consumed by the SM capacitors on the j-leg in a fundamental cycle should be kept at zero to balance the transferred power between ac and dc systems. According to (9), the average power of each phase leg of MMC can be adjusted by injecting the dc-circulating current so that the balance of leg SMs capacitor voltage can be realized. Then, the dc circulating currents of MMC are given as follows:

$$\begin{cases} i_{\rm dca} = i_{\rm dc}/3 + \Delta i_{\rm dca} = \frac{1}{2U_{\rm dc}} \\ \qquad \times \begin{bmatrix} E^+I^+\cos(\theta^+ - \varphi^+) - E^-I^+\cos(\theta^- + \varphi^+) \\ +E^0I^+\cos(\theta^0 - \varphi^+) \end{bmatrix} \\ i_{\rm dcb} = i_{\rm dc}/3 + \Delta i_{\rm dcb} = \frac{1}{2U_{\rm dc}} \\ \quad \times \begin{bmatrix} E^+I^+\cos(\theta^+ - \varphi^+) - E^-I^+\cos(\theta^- + \varphi^+ + 120^\circ) \\ +E^0I^+\cos(\theta^0 - \varphi^+ + 120^\circ) \end{bmatrix} \\ i_{\rm dcc} = i_{\rm dc}/3 + \Delta i_{\rm dcc} = \frac{1}{2U_{\rm dc}} \\ \quad \times \begin{bmatrix} E^+I^+\cos(\theta^+ - \varphi^+) - E^-I^+\cos(\theta^- + \varphi^+ - 120^\circ) \\ +E^0I^+\cos(\theta^0 - \varphi^+ - 120^\circ) \end{bmatrix}. \end{cases} \tag{10}$$

From (10), the following constraint in (11) always remains satisfied, which means that the two control degree-of-freedom (DOF) of dc-circulating current are needed

$$i_{\rm dca} + i_{\rm dcb} + i_{\rm dcc} = I_{\rm dc}. \tag{11}$$

2) The average power flow analysis based on negative-sequence current injection.

The average power flow analysis based on negative-sequence current injection was performed and demonstrated. When MMC uses a negative-sequence current injection method to regulate the leg voltage, three-phase dc circulating currents remain equal, i.e., $i_{\rm dca} = i_{\rm dcb} = i_{\rm dcc} = i_{\rm dc}/3$. The three-phase average powers with a negative-sequence current injection can be rewritten as follows:

$$\begin{cases} 2P_a^{\sum} = \bar{P} - E^-I^+\cos(\theta^- + \varphi^+) + E^0I^+\cos(\theta^0 - \varphi^+) \\ \qquad -E^+I^-\cos(\theta^+ + \varphi^-) - E^0I^-\cos(\theta^0 + \varphi^-) \\ 2P_b^{\sum} = \bar{P} - E^-I^+\cos(\theta^- + \varphi^+ + 120^\circ) \\ \qquad +E^0I^+\cos(\theta^0 - \varphi^+ + 120^\circ) - E^+I^-\cos(\theta^+ + \varphi^- \\ \qquad +120^\circ) - E^0I^-\cos(\theta^0 + \varphi^- - 120^\circ) \\ 2P_c^{\sum} = \bar{P} - E^-I^+\cos(\theta^- + \varphi^+ - 120^\circ) \\ \qquad +E^0I^+\cos(\theta^0 - \varphi^+ - 120^\circ) - E^+I^-\cos(\theta^+ + \varphi^- \\ \qquad -120^\circ) - E^0I^-\cos(\theta^0 + \varphi^- + 120^\circ) \end{cases} \tag{12}$$

where $\bar{P} = -2U_{\rm dc}i_{\rm dc}/3 + E^+I^+\cos(\theta^+ - \varphi^+) + E^-I^-\cos(\theta^- - \varphi^-)$.

Equation (12) shows that the sum of the three-phase average power $P_{{\rm pn}j}$ and $P_{0{\rm n}j}$ generated by a combination of positive- and zero-sequence voltage with a negative-sequence current is kept at zero. Therefore, the average power of each phase leg of MMC can also be adjusted by injecting the negative-sequence current.

Furthermore, by making difference of the MMC arm instantaneous power $p_{{\rm p}j}$ and $p_{{\rm n}j}$, one can be obtained

$$\begin{aligned} p_a^{\Delta} &= p_{pa} - p_{na} = -0.5U_{\rm dc}[I^+\sin(\omega_1 t + \varphi^+) \\ &\quad + I^-\sin(-\omega_1 t + \varphi^-)] + 2i_{\rm dca}[E^+\sin(\omega_1 t + \theta^+) \\ &\quad + E^-\sin(-\omega_1 t + \theta^-) + E^0\sin(\omega_1 t + \theta^0)] \end{aligned} \tag{13}$$

$$\begin{aligned} p_b^{\Delta} &= -0.5U_{\rm dc}\begin{bmatrix} I^+\sin(\omega_1 t + \varphi^+ - 120^\circ) \\ +I^-\sin(-\omega_1 t + \varphi^- - 120^\circ) \end{bmatrix} \\ &\quad + 2i_{\rm dcb}\begin{bmatrix} E^+\sin(\omega_1 t + \theta^+ - 120^\circ) \\ +E^-\sin(-\omega_1 t + \theta^- - 120^\circ) \\ +E^0\sin(\omega_1 t + \theta^0) \end{bmatrix} \end{aligned} \tag{14}$$

$$\begin{aligned} p_c^{\Delta} &= -0.5U_{\rm dc}\begin{bmatrix} I^+\sin(\omega_1 t + \varphi^+ + 120^\circ) \\ +I^-\sin(-\omega_1 t + \varphi^- + 120^\circ) \end{bmatrix} \\ &\quad + 2i_{\rm dcc}\begin{bmatrix} E^+\sin(\omega_1 t + \theta^+ + 120^\circ) \\ +E^-\sin(-\omega_1 t + \theta^- + 120^\circ) \\ +E^0\sin(\omega_1 t + \theta^0) \end{bmatrix}. \end{aligned} \tag{15}$$

It can be seen that whether the ac grid voltage is symmetrical or not, the difference between the instantaneous power of the upper and lower arms always presents a fundamental frequency fluctuation. Due to the existence of zero-sequence voltage, the asymmetry of instantaneous power $p_a^{\Delta}, p_b^{\Delta}, p_c^{\Delta}$ cause the zero-sequence ac circulating current if not controlled, which leads to high zero-sequence currents in ac-side and dc-bus.

From (6)–(15), several key points are concluded as follows.

1) From (6)–(8), there are six DOFs in terms of the positive-, negative-sequence ac-side currents, and dc circulating currents. If one would like to realize the dc-bus voltage/power and reactive power control, two of them should be reserved for these objectives, and there are still four DOFs left for other usages as described below.
2) From (9) and (11), two DOFs about dc circulating currents can be utilized for leg-averaging control. However, it is also observed that the balance of leg SMs capacitor voltage by injecting the dc-circulating current is only valid when

the MMC synthesizes the dc-bus voltage. The control DOFs with the dc-circulating current injection method is not able to balance the leg SMs capacitor voltage during the pole-to-pole short-circuit FRT period.

3) The combination of positive- and zero-sequence voltage with a negative-sequence current at a, b, c phases is zero as in (12), which means that the leg-balancing control with negative-sequence current needs only two DOFs.
4) From (13)–(15), under asymmetrical faults in the transformer-less MMC scheme, there will be a considerable zero-sequence component in grid voltage, which leads to high zero-sequence currents in ac-side and dc-side.

Moreover, in the practical, there may be a certain difference in upper and lower arm parameters, and even a slight mismatch in parameters will lead to the deviation of the stored energy, which leads to increased and distorted circulating currents [7], [9]. Besides, in medium-voltage applications, the number of submodules per arm is relatively small, where the impact of dead time negatively influences on ac-side current harmonics, dc-bus voltage ripple, and circulating harmonics currents [37].

III. Proposed Improved Comprehensive Control of MMC

In fact, from (1) and (2), it can be observed that the arm voltage $u_{\mathrm{p}j}$, $u_{\mathrm{n}j}$ can be decomposed to the controllable dc voltage source ($u_{\mathrm{dcp}j}$, $u_{\mathrm{dcn}j}$), fundamental frequency ac voltage source ($u_{\mathrm{acp}j}$, $u_{\mathrm{acn}j}$), and ac-component circulating voltage source ($u_{\mathrm{zacp}j}$, $u_{\mathrm{zacn}j}$), which can be expressed as

$$\begin{cases} u_{\mathrm{acp}j} = \frac{L}{2}\frac{\mathrm{d}i_j}{\mathrm{d}t} + R\frac{i_j}{2} - u_{\mathrm{s}j} \\ u_{\mathrm{dcp}j} = \frac{U_{\mathrm{dc}}}{2} + u_{o'o} + L\frac{\mathrm{d}i_{\mathrm{dc}j}}{\mathrm{d}t} + Ri_{\mathrm{dc}j} \\ u_{\mathrm{zacp}j} = L\frac{\mathrm{d}i_{\mathrm{zac}j}}{\mathrm{d}t} + Ri_{\mathrm{zac}j}. \end{cases} \tag{16}$$

Hence, the decoupling model of upper and lower arms depending on different components is shown in Fig. 3. Clearly, it can be found that the different frequencies currents (ac-side current, dc- and ac-component circulating currents) via arm current control are effectively realized with the comprehensive control instead of using the conventional current control strategy.

To realize both ac/dc FRT and multifrequency harmonics suppression, an improved comprehensive control strategy, including the hierarchical voltage control and arm current control, is needed to be accomplished with the following four control objectives:

1) obtain ac fault ride through capability;
2) obtain dc fault ride through capability and support ac grid as a static synchronous compensator;
3) secure the MMC through leg-averaging and arm-balancing voltage control;
4) eliminate the multifrequency harmonics at dc-bus voltage, ac-side current, and undesired circulating currents.

In this article, the proposed improved comprehensive control architecture of MMC is shown in Fig. 4, which mainly consists of three parts: 1) outer-loop hierarchical voltage control, 2) inner-loop RC-based arm current control, and 3) modulation

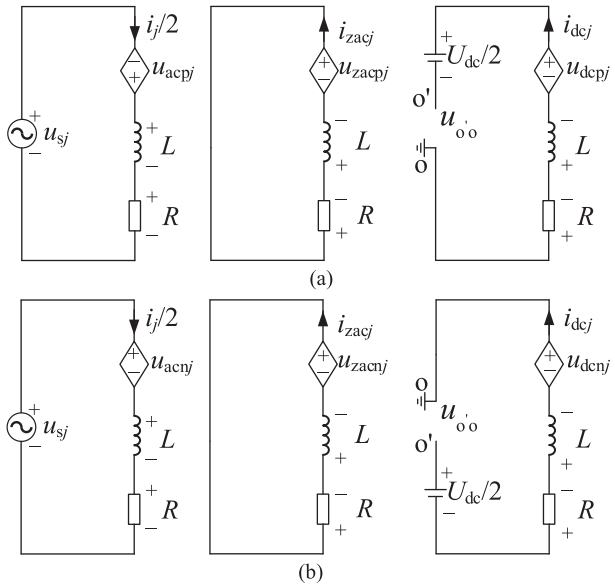

Fig. 3. Decoupling model of upper and lower arms. (a) Decoupling model of upper arm. (b) Decoupling model of lower arm.

(including individual balancing control). The outer-loop hierarchical voltage control includes dc-bus voltage/power control, leg-averaging control, arm-balancing control, individual balancing control, and positive-sequence phase-locked loop (PS-PLL). The inner loop is responsible for controlling the arm currents to track their corresponding references. The modulation loop is responsible for generating the switching signals for the submodules.

The proposed scheme focuses on hierarchical voltage control and RC-based arm current control, which can well adapt to various operating conditions such as ac and dc grid faults, ac grid voltage distortion, arm parameters asymmetry, and dead time. It also ensures the high quality of voltage and current at both ac-side and dc-side of MMC system. The proposed comprehensive control strategy can control the MMC without decomposing the positive-, negative-, and zero-sequence of ac-side currents and arm currents, and does not involve any separate circulating current controller design; eventually, it improves the operation reliability of MMC.

The detailed outer-loop improved hierarchical voltage control, and inner-loop RC-based arm current control are presented in the following Section IV and Section V, respectively.

IV. Improved Hierarchical Voltage Control

The outer-loop voltage control plays a vital role in obtaining high performance control and stable operation of MMC. The hierarchical voltage control of MMC in this article can be categorized into: 1) dc-bus voltage/power control; 2) leg-averaging control; 3) arm-balancing control; and 4) individual-balancing control.

A. DC-Bus Voltage/power Control

The dc-bus voltage/power control strategy is focused on the dc-bus voltage U_{dc}^* or power P_{dc}^*. In the first scenario of dc-bus

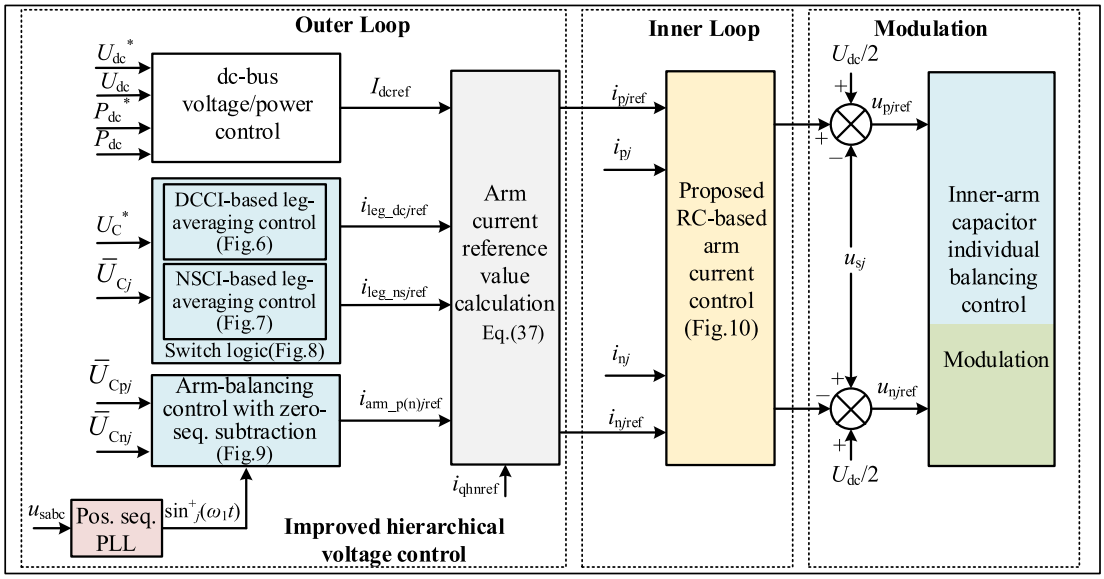

Fig. 4. Proposed improved comprehensive control architecture of MMC based on the improved hierarchical capacitor voltage control and the RC-based arm current control.

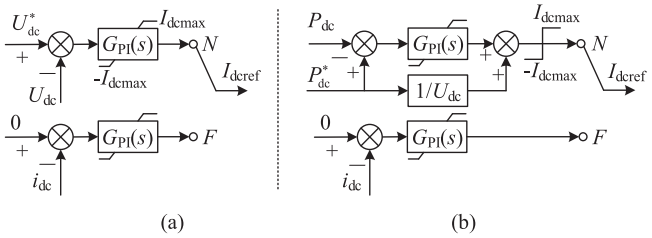

Fig. 5. Block diagram of dc-bus voltage/power control. (a) DC-bus voltage control. (b) Power control.

voltage, the control block diagram is shown in Fig. 5(a) and the dc-bus reference current can be obtained

$$I_{\mathrm{dcref}} = \left(K_{\mathrm{dc\_p}} + K_{\mathrm{dc\_i}}/s\right)\left(U_{\mathrm{dc}}^{*} - U_{\mathrm{dc}}\right). \tag{17}$$

Considering the power P_{dc}^{*}, the outer-loop power control block diagram is reflected in Fig. 5(b), where the PI regulator has added to eliminate the tracking error as

$$I_{\mathrm{dcref}} = \left(K_{\mathrm{dc\_p}} + K_{\mathrm{dc\_i}}/s\right)\left(P_{\mathrm{dc}}^{*} - P_{\mathrm{dc}}\right) + P_{\mathrm{dc}}^{*}/U_{\mathrm{dc}}. \tag{18}$$

When the pole-to-pole dc fault happens and the dc-bus voltage drops to zero, the dc-bus voltage/power control as in (17) or (18) (Normal operation, *N*) should switch to the dc-bus current control (Fault operation, *F*) as in Fig. 5. The dc-bus current should be controlled to zero for extinguishing arc and the fault isolation in case of permanent faults [16]–[19], [38]–[40]. As soon as the dc fault is cleared, the MMC is able to resume operation at their prefault state, after the dc-bus voltage is ramped up to its nominal level through the internal control operation of the MMC [16]–[18], [38], [39]. In the meantime, the reactive power compensation is better achieved by the MMC during the fault clearance operation, especially when the stability of the system is required [40].

B. Leg-Averaging Control

The purpose of the leg-averaging control scheme is to ensure the average value of floating dc-capacitor in each leg tracking the reference value. Considering the three-phase voltage asymmetry and the imbalance loss, leg-averaging control can be achieved by adjusting the dc-circulating current or injecting the negative-sequence current. Two solution approaches are proposed in this article, namely, DCCI-based and NSCI-based leg-averaging control, which can switch seamlessly. The explanation of both methods is presented as follows.

1) DCCI-Based Leg-Averaging Control: Considering the double frequency fluctuation in MMC leg average voltage, in case of nonfiltering, the output of leg-averaging control will contain the double frequency ripple component, and it consequently appears in the current loop. Therefore, to remove the ripple components, a 100 Hz notch filter has introduced in the feedback loop, and the average value of the leg voltage can be expressed as

$$\bar{U}'_{Cj} = \frac{1}{2N_c}\left(\sum_{i=1}^{N_c} u_{\mathrm{Cp}ji} + \sum_{i=1}^{N_c} u_{\mathrm{Cn}ji}\right)\frac{s^2+\omega_2^2}{s^2+2\tau\omega_2 s+\omega_2^2} \tag{19}$$

where ω_2 is the double-frequency angular frequency and τ is the notch filter parameter. $u_{\mathrm{Cp}ji}$ and $u_{\mathrm{Cn}ji}$ are the upper and lower arm *i*th SM capacitor voltage of *j*-phase, respectively.

Then, the current command $\triangle I_{\mathrm{leg\_}j}$ is produced by the PI regulator in the leg-averaging control

$$\Delta I_{\mathrm{leg\_}j} = \left(K_{\mathrm{leg\_p}} + K_{\mathrm{leg\_i}}/s\right)\left(U_{\mathrm{C}}^{*} - \bar{U}'_{\mathrm{C}j}\right). \tag{20}$$

In order to ensure the balance of ac-side three-phase current symmetry under grid voltage asymmetry conditions, the average output value of the three-phase leg-averaging PI regulator is taken as the command amplitude of the ac-side current, as shown

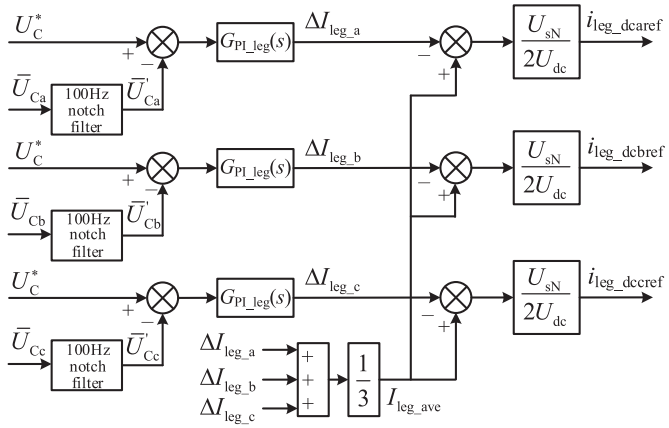

Fig. 6. Block diagram of DCCI-based leg-averaging control.

in

$$I_{\text{leg\_ave}} = \frac{1}{3}\left(\Delta I_{\text{leg\_}a} + \Delta I_{\text{leg\_}b} + \Delta I_{\text{leg\_}c}\right). \tag{21}$$

Moreover, to sustain the total active power of MMC, the dc-circulating current reference for each leg can be modified as follows:

$$\begin{aligned} I_{\text{dc}j\text{ref}} &= \frac{1}{3} I_{\text{dcref}} + i_{\text{leg\_dc}j\text{ref}} \\ &= \frac{1}{3} I_{\text{dcref}} + \frac{U_{\text{sN}}}{2U_{\text{dc}}}\left(I_{\text{leg\_ave}} - \Delta I_{\text{leg\_}j}\right) \end{aligned} \tag{22}$$

where U_{sN} is the positive-sequence amplitude of the ac grid voltage. Equation (22) realizes the capacitor average voltage of a leg balanced with its rated value, as the dc-circulating current commands of each phase are no longer equal, which are updated according to the deviation. Since

$$I_{\text{dcaref}} + I_{\text{dcbref}} + I_{\text{dccref}} = I_{\text{dcref}}. \tag{23}$$

The updated dc-circulating currents have no effect on the total output active power of MMC, as reflected in the block diagram of leg-averaging control in Fig. 6.

2) NSCI-Based Leg-Averaging Control: A leg capacitor voltage averaging control method based on the negative-sequence current can be used, in addition to the DCCI-based method. Different from the existing methods [20], [41], this section introduces a new idea of leg-averaging control based on the negative-sequence current injection. From (12), an averaging component of the active power of three phases induced by positive- and zero-sequence voltage with negative-sequence current can be obtained as

$$\begin{cases} \bar{P}_{\text{a\_p0n}} = -\frac{1}{2}E^+I^-\cos(\theta^+ + \varphi^-) - \frac{1}{2}E^0I^-\cos(\theta^0 + \varphi^-) \\ \bar{P}_{\text{b\_p0n}} = -\frac{1}{2}E^+I^-\cos(\theta^+ + \varphi^- + 120^\circ) \\ \qquad -\frac{1}{2}E^0I^-\cos(\theta^0 + \varphi^- - 120^\circ) \\ \bar{P}_{\text{c\_p0n}} = -\frac{1}{2}E^+I^-\cos(\theta^+ + \varphi^- - 120^\circ) \\ \qquad -\frac{1}{2}E^0I^-\cos(\theta^0 + \varphi^- + 120^\circ). \end{cases} \tag{24}$$

From (24), the following constraints can be obtained:

$$\begin{cases} \bar{P}_{\text{a\_p0n}} + \bar{P}_{\text{b\_p0n}} + \bar{P}_{\text{c\_p0n}} = 0 \\ \bar{P}_{\text{a\_p0n}} = -\frac{1}{2}E^+I^-\cos(\theta^+ + \varphi^-) - \frac{1}{2}E^0I^-\cos(\theta^0 + \varphi^-) \\ \bar{P}_{\text{b\_p0n}} - \bar{P}_{\text{c\_p0n}} = \frac{\sqrt{3}}{2}E^+I^-\sin(\theta^+ + \varphi^-) \\ \qquad -\frac{\sqrt{3}}{2}E^0I^-\sin(\theta^0 + \varphi^-). \end{cases} \tag{25}$$

On the other hand, the negative-sequence current in dq-frame can be expressed as

$$\begin{aligned} \begin{bmatrix} I_{\text{nd}} \\ I_{\text{nq}} \end{bmatrix} &= C^-_{\text{abc-dq}} \begin{bmatrix} I^-\sin(-\omega_1 t + \varphi^-) \\ I^-\sin(-\omega_1 t + \varphi^- - 120^\circ) \\ I^-\sin(-\omega_1 t + \varphi^- + 120^\circ) \end{bmatrix} \\ &= \begin{bmatrix} I^-\cos(\varphi^-) \\ I^-\sin(\varphi^-) \end{bmatrix} \end{aligned} \tag{26}$$

where

$$\begin{aligned} &C^-_{\text{abc-dq}} \\ &= \frac{2}{3}\begin{bmatrix} \sin(-\omega_1 t) & \sin(-\omega_1 t - 120^\circ) & \sin(-\omega_1 t + 120^\circ) \\ \cos(-\omega_1 t) & \cos(-\omega_1 t - 120^\circ) & \cos(-\omega_1 t + 120^\circ) \end{bmatrix}. \end{aligned}$$

Considering that the voltage drop of MMC output current on the arm inductor is much smaller than the ac grid voltage, there is $\theta^+ \approx 0$. Substituting (26) into (25), the relationship between negative-sequence current and power of MMC can be approximately expressed as follows:

$$\begin{cases} \bar{p}_{\text{a\_p0n}} \approx -\frac{1}{2}\left(E^+ + E^0\cos\theta^0\right) I_{\text{nd}} + \frac{1}{2}E^0 I_{\text{nq}}\sin\theta^0 \\ \bar{p}_{\text{b\_p0n}} - \bar{p}_{\text{c\_p0n}} \approx \frac{\sqrt{3}}{2}\left(E^+ - E^0\cos\theta^0\right) I_{\text{nq}} \\ \qquad -\frac{\sqrt{3}}{2}E^0 I_{\text{nd}}\sin\theta^0. \end{cases} \tag{27}$$

In (27), the zero-sequence components are nonsexist if a $\triangle$-connection transformer is utilized, then the *d*- and *q*-axis in (27) are decoupled. In a transformer-less scheme, the coupling terms $0.5E^0 I_{\text{nq}}\sin\theta^0$ and $-\sqrt{3}E^0 I_{\text{nd}}(\sin\theta^0)/2$ can be treated as coupling disturbances, and the tracking error can be eliminated by PI regulator. Therefore, the power of a-phase leg of MMC can be adjusted by injecting the negative-sequence current in *d*-axis component i_{nd}; the power of b-phase and c-phase legs can be adjusted by injecting the negative-sequence current in *q*-axis component i_{nq}.

Fig. 7 shows the block diagram of NSCI-based leg-averaging control proposed in this article. First, a PI regulator is employed to force the overall average voltage of three legs $\bar{U}'_C$ to follow the command voltage U^*_{C}

$$\Delta I_{\text{leg}} = \left(U^*_{\text{C}} - \bar{U}'_{\text{C}}\right)\left(K_{\text{leg\_p}} + K_{\text{leg\_i}}/s\right). \tag{28}$$

Then, according to (27), a PI regulator is used to adjust the negative-sequence current in *d*-axis component for balancing a-leg power, while a PI regulator is used to adjust the negative-sequence current in *q*-axis component for balancing b-leg and c-leg power. One can obtain as

$$\Delta I_{\text{leg\_nd}} = \left(\bar{U}'_{\text{Ca}} - \bar{U}'_{\text{C}}\right)\left(K_{\text{leg\_p}} + K_{\text{leg\_i}}/s\right) \tag{29}$$

$$\Delta I_{\text{leg\_nq}} = -\left(\bar{U}'_{\text{Cb}} - \bar{U}'_{\text{Cc}}\right)\left(K_{\text{leg\_p}} + K_{\text{leg\_i}}/s\right). \tag{30}$$

Finally, the injected negative-sequence current in abc-frame can be obtained with negative inverse transformation $C^-_{\text{dq-abc}}$.

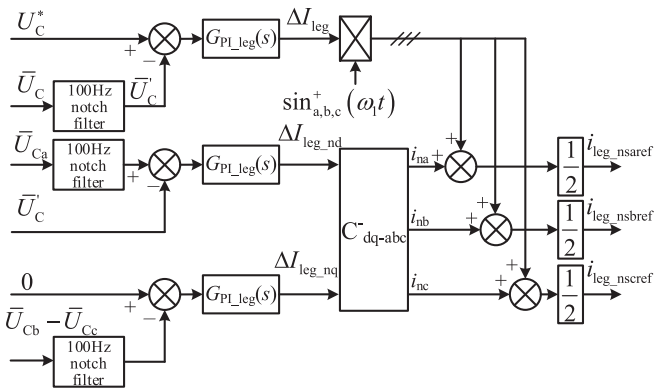

Fig. 7. Block diagram of the proposed NSCI-based leg-averaging control.

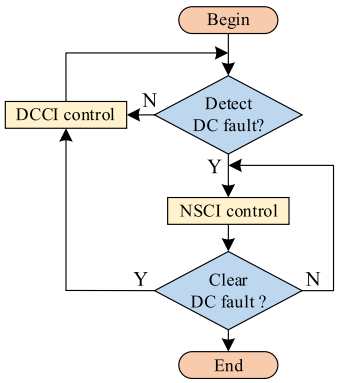

Fig. 8. Switch logic between NSCI control and DCCI control under ac and dc fault-ride through.

The output reference current of NSCI-based leg-averaging control can be obtained as

$$\begin{bmatrix} i_{\text{leg\_nsaref}} \\ i_{\text{leg\_nsbref}} \\ i_{\text{leg\_nscref}} \end{bmatrix} = \frac{1}{2}\left\{ \begin{bmatrix} \Delta I_{\text{leg}} \sin^+(\omega_1 t) \\ \Delta I_{\text{leg}} \sin^+(\omega_1 t - 120^\circ) \\ \Delta I_{\text{leg}} \sin^+(\omega_1 t + 120^\circ) \end{bmatrix} + C^-_{\text{dq-abc}} \begin{bmatrix} \Delta I_{\text{leg\_nd}} \\ \Delta I_{\text{leg\_nq}} \end{bmatrix} \right\}. \tag{31}$$

It should be noted that the essence of leg-averaging control is the process of power redistribution among three legs, which does not affect on the total dc output power of the MMC. In other words, (23) and (25) always remain satisfied. In addition, it should also be emphasized that the DCCI-based leg averaging approach is invalid during the pole to pole short-circuit fault ride through. In such a scenario, it is important to seamlessly switch to the proposed NSCI-based leg-averaging control. Consequently, since the magnitude of the negative-sequence current injected is very small and disappears under normal operating conditions, the proposed NSCI leg-averaging control is valid and is perceived as a promising solution both for the ac and dc fault ride through. The proposed NSCI-based leg-averaging control can be integrated together with DCCI control by seamlessly switching operation during the ac and dc grid faults, as shown in Fig. 8. The obtained experimental results of the switching operation are illustrated in Fig. 32.

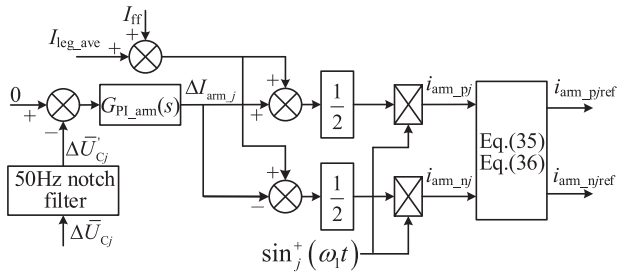

Fig. 9. Block diagram of arm-balancing control and zero-sequence current subtraction.

C. Arm-Balancing Control and Zero-Sequence Current Subtraction

Generally, the output of arm-balancing control contains the ripple components; therefore, a 50 Hz notch filter should be introduced in the feedback loop to remove the ripples, and the difference of the average value of the arm voltage can be expressed as

$$\Delta \bar{U}'_{Cj} = \frac{1}{N_c}\left(\sum_{i=1}^{N_c} u_{\text{Cp}ji} - \sum_{i=1}^{N_c} u_{\text{Cn}ji}\right) \frac{s^2+\omega_1^2}{s^2+2\tau\omega_1 s+\omega_1^2}. \tag{32}$$

Then, the current command $\triangle I_{\text{arm\_}j}$ is produced by the PI regulator in the arm-balancing control

$$\Delta I_{\text{arm\_}j} = \left(K_{\text{arm\_p}} + K_{\text{arm\_i}}/s\right)\left(0 - \Delta \bar{U}'_{Cj}\right). \tag{33}$$

Furthermore, in order to improve the dynamic response, the feed-forward I_{ff} is introduced. According to the conservation of ac and dc power, one can be obtained as

$$I_{\text{ff}} = 2U_{\text{dc}} I_{\text{dcref}}/(3U_{\text{sN}}). \tag{34}$$

The control block diagram of the arm-balancing control can be attained, as shown in Fig. 9. It should be noted that the three-phase PS-PLL has to be employed to guarantee the symmetrical ac-side three-phase currents under the harmonic and phasors asymmetry of grid voltage.

In order to suppress the zero-sequence circulating current caused by the zero-sequence voltage of ac grid and the imbalance loss among the three legs, which will result in large ripple at dc-bus voltage if not controlled, the following zero-sequence current subtraction is carried out:

$$\begin{cases} i_{\text{arm\_pzero}} = (i_{\text{arm\_pa}} + i_{\text{arm\_pb}} + i_{\text{arm\_pc}})/3 \\ i_{\text{arm\_nzero}} = (i_{\text{arm\_na}} + i_{\text{arm\_nb}} + i_{\text{arm\_nc}})/3. \end{cases} \tag{35}$$

By subtracting the zero-sequence component from the arm currents, we can get

$$\begin{cases} i_{\text{arm\_p}j\text{ref}} = i_{\text{arm\_p}j} - i_{\text{arm\_pzero}} \\ i_{\text{arm\_n}j\text{ref}} = i_{\text{arm\_n}j} - i_{\text{arm\_nzero}}. \end{cases} \tag{36}$$

D. Individual-Balancing Control

Individual-balancing control is the same as proposed in [42].

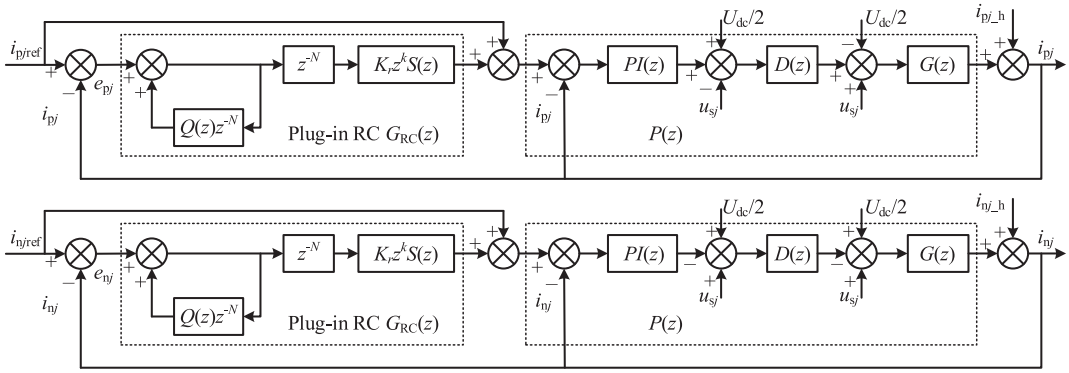

Fig. 10. Block diagram of the proposed arm current control based on repetitive controller.

V. Proposed RC-Based Arm Current Control

Based on the abovementioned analysis, the inner-loop arm current reference based on seamlessly switching operation of DCCI-and NSCI-based leg-averaging control can be achieved as

$$\begin{cases} i_{pjref} = +\frac{1}{3}I_{dcref} + Ki_{leg\_dcjref} + (1-K)i_{leg\_nsjref} \\ \qquad\quad +i_{arm\_pjref} + i_{qhnref} \\ i_{njref} = -\frac{1}{3}I_{dcref} - Ki_{leg\_dcjref} + (1-K)i_{leg\_nsjref} \\ \qquad\quad +i_{arm\_njref} + i_{qhnref} \end{cases} \tag{37}$$

where $I_{dcref}/3$ is the output of the overall voltage/power controller. i_{leg_dcjref} is the output of the DCCI-based leg-averaging control. i_{leg_nsjref} is the output of the NSCI-based leg-averaging control. K ($K = 1$ or $K = 0$) is the weight factor. $K = 1$ and $K = 0$ correspond to DCCI and NSCI control, respectively. $i_{arm\_p(n)jref}$ indicates the output of the arm-balancing control. i_{qhnref} is the command current for reactive current compensation, harmonic current suppression, and negative current compensation for power quality control.

The inner-loop current reference can be obtained through the outer-loop voltage control described in (37), which is suitable for various operating conditions. However, it is observed that the arm current reference values i_{pjref} and i_{njref} contain dc-component and ac-component currents. Besides, the disturbances caused by ac grid voltage distortion and dead time effect are multifrequency periodic harmonic disturbances [37]. The repetitive control method based on the internal model principle with a high gain of frequencies has been widely used in the ac/dc converter. However, the presented RC for MMC in [25] and [31]–[36] only realizes the even-order circulating current suppression function. It neither realizes the zero-tracking error of the periodic ac-side command signals nor eliminates the influence of the grid voltage distortion and dead time effect on the ac-side current harmonic [37]. Therefore, the arm current control combined with the repetitive controller is proposed to eliminate both even-order and odd-order harmonics at arm current. The significant outcomes of the proposed RC-based arm current control are as follows:

1) it is able to track the arm current reference accurately;
2) it can effectively suppress a series of undesirable multifrequency circulating currents;
3) it can eliminate all the multifrequency harmonics at ac-side currents, arm currents, and dc-bus voltage.

A. Proposed Repetitive Controller-Based Arm Current Control

The block diagram of the proposed repetitive controller-based arm current control is shown in Fig. 10, where the $i_{p(n)jref}$ is the reference values of upper and lower arm currents as expressed in (37), $i_{p(n)j}$ is the actual arm currents, and $i_{p(n)j\_h}$ is the disturbance harmonic currents. $D(z)$ is the time delay of the control system, i.e., $D(z) = z^{-1}$. $G(z)$ is the controlled plant of the upper and lower arm, which can be expressed as

$$G(z) = \frac{T_s\left(1+z^{-1}\right)}{2L\left(1-z^{-1}\right) + RT_s\left(1+z^{-1}\right)} \tag{38}$$

where T_s is the sampling time of the control system.

Since the tracking error is eliminated by repetitive control, the PI controller can be simplified to proportional control, i.e., $\mathrm{PI}(z) = K_p$. The transfer function of the repetitive controller is expressed as

$$G_{RC}(z) = \frac{K_r S(z) z^{-N+k}}{1 - Q(z)z^{-N}} \tag{39}$$

where $N = f_s/f_1$, f_s is the sampling frequency, and f_1 is the fundamental frequency; and K_r is the gain of the repetitive controller. The filter $Q(z)$ is used to enhance the stability of the repetitive controller, which can be selected as a low-pass filter or constant slightly less than 1; z^k is the leading compensation to compensate the time delay caused by the controller and the controlled plant; and $S(z)$ is the low-pass filter to enhance the stability of the controller.

For further simplification, (z) has been removed for the following transfer functions. According to Fig. 10, the ac-side and dc-side voltage disturbances u_{sj} and U_{dc} can be aggregated into the disturbance harmonic currents $i_{p(n)j\_h}$, then the transfer function of output current and tracking error of arm current are expressed as follows:

$$\begin{aligned} i_{pj} = & \frac{P\left(1 - Qz^{-N} + K_r S z^{-N+k}\right)}{1 - Qz^{-N} + PK_r S z^{-N+k}} i_{pjref} \\ & + \frac{1}{(1+K_p DG)} \frac{\left(1 - Qz^{-N}\right)}{1 - Qz^{-N} + PK_r S z^{-N+k}} i_{pj\_h} \end{aligned} \tag{40}$$

$$e_{\mathrm{p}j} = \frac{\left(1-Qz^{-N}\right)(1-P)}{1-Qz^{-N}+PK_rSz^{-N+k}} i_{\mathrm{p}j\mathrm{ref}} - \frac{1}{(1+K_pDG)} \frac{\left(1-Qz^{-N}\right)}{1-Qz^{-N}+PK_rSz^{-N+k}} i_{\mathrm{p}j\_\mathrm{h}} \tag{41}$$

where $P = K_{\mathrm{p}}DG/(1 + K_{\mathrm{p}}DG)$.

In order to ensure the stability of the arm current controller, the following two conditions shall be satisfied.

1) Without the inclusion of repetitive controller, the equivalent controlled plant P must be stable.
2) $|H| = |Q - PK_rSz^k| < 1, \forall z = e^{j\omega T_s}, 0 < \omega < \pi/T_s$.

According to the error transfer (41), the tracking error comprises the reference current tracking error and harmonics disturbance error, where the harmonic disturbances currents include the grid voltage harmonics and dead-time effect. Since $z^{-N} = 1$, (41) is transformed into the frequency domain with $z = e^{j\omega Ts}$, and the amplitude expression of the current tracking error can be written as

$$\left|e_{\mathrm{p}j}(e^{j\omega T_s})\right| = \left|\frac{1-Q(e^{j\omega T_s})}{1-H(e^{j\omega T_s})}\right| \left|\left(1-P(e^{j\omega T_s})\right) i_{\mathrm{p}j\mathrm{ref}}(e^{j\omega T_s})\right| - \left|\frac{1-Q(e^{j\omega T_s})}{1-H(e^{j\omega T_s})}\right| \left|\frac{1}{(1+K_pDG)} i_{\mathrm{p}j\_\mathrm{h}}(e^{j\omega T_s})\right|. \tag{42}$$

Because the reference currents and harmonic currents are periodic, one can be obtained

$$\begin{cases} i_{\mathrm{p}j\mathrm{ref}}(z) = i_{\mathrm{p}j\mathrm{ref}}(z)\, z^{-N} \\ i_{\mathrm{p}j\_\mathrm{h}}(z) = i_{\mathrm{p}j\_\mathrm{h}}(z)\, z^{-N}. \end{cases} \tag{43}$$

Substituting (43) into (41), we can get [34]

$$z^N e_{\mathrm{p}j}(z) = H(z)\, e_{\mathrm{p}j}(z). \tag{44}$$

From (42) and (44), the key findings can be concluded as follows.

1) From (42), it can be observed that the adaption of the repetitive control strategy eliminates the harmonics and keeps the steady-state tracking error at zero. For instance, the reference current signal tracking error and harmonic suppression error are attenuated to $|\frac{1-Q(e^{j\omega T_s})}{1-H(e^{j\omega T_s})}|$ times of the original (without repetitive control). In an ideal case, $Q(z) = 1$, and $|\frac{1-Q(e^{j\omega T_s})}{1-H(e^{j\omega T_s})}| = 0$, it demonstrates that the harmonics in the $0 \sim f_{\mathrm{s}}/2$ band are totally suppressed, and the steady-state tracking error would be zero.
2) Equation (44) identifies that after each fundamental frequency period, the tracking error is reduced to $|H(e^{j\omega T_s})|$ times of the previous one, which proves the robust convergence speed. Moreover, in an ideal case, $Q(z) = 1$, $PK_{\mathrm{r}}Sz^k = 1\angle 0^\circ$, then $|H(e^{j\omega T_s})| = 0$, indicating that the tracking error or harmonic suppression error in the $0 \sim f_{\mathrm{s}}/2$ will be eliminated in the next fundamental frequency period.

B. Robustness Analysis and Parameter Design

To evaluate the robustness of the proposed RC-based arm current control and the parameter design, the simulation and experimental parameters of three-phase MMC system are presented in Table I. The experimental parameters are being used to design and analyze the performance of the proposed RC-based arm current control.

TABLE I
SIMULATION AND EXPERIMENTAL PARAMETERS OF THREE-PHASE MMC

Parameters	Simulation Value	Experimental value
Grid voltage(line-to- line)u_{sab}/V	10000	190
Fundamental frequency f_{l}/Hz	50	50
dc-bus voltage U_{dc}/V	20000	400
Module count N_{c}	10	2
dc-capacitor voltage U_{sm}/V	2000	200
dc capacitance C_{sm}/mF	2	6
Arm inductance L/mH	40	10
Switching frequency f_{sw}/Hz	1000	5000
Equivalent switching freq./kHz	20	20
Sampling frequency f_{s}/kHz	10	10

It can be seen from Fig. 10 that the RC comprises an internal model, fundamental period delay $z^{-N,}$ and compensator $K_{\mathrm{r}}Sz^k$. The fundamental period delay z^{-N} can be determined from the sampling frequency of the control system. In this article, the sampling frequency f_{s} is equal to 10 kHz, which means N is equal to 200. In practical application, the internal model parameter $Q(z)$ of RC is usually chosen as a low-pass filter or constant slightly less than 1. In order to simplify the controller, the value of $Q(z)$ is taken as 0.97. The $S(z)$ is generally a low-pass filter for the RC stability enhancement to suppress the influence of high-frequency noise on the steady-state tracking error. To avoid the extra phase lag introduced by low-pass filter $S(z)$, zero phase-shift low-pass filter (ZPF) is adopted in this article and the generic form can be expressed as

$$S(z) = \sum_{i=1}^{m} \alpha_i z^i + \alpha_0 + \sum_{i=1}^{m} \alpha_i z^{-i} \tag{45}$$

where $\alpha_0 + 2\sum_{i=1}^{m} \alpha_i = 1$, m is a positive integer, which is the order of the ZPF, and the higher order of m enhances the filtering quality. However, due to the complex form of ZPF, the first-order low-pass filter has implemented for simplification, and it can be expressed as

$$S(z) = 0.25z + 0.5 + 0.25z^{-1}. \tag{46}$$

In order to compensate the phase lag of the equivalent controlled plant $P(z)$, z^k is used for phase compensation and the obtained Bode diagram of $z^kP(z)$ using different values of k, as shown in Fig. 11. Clearly, it can be seen that when $k = 3$, the lead compensation can cancel the phase lag of the equivalent controlled plant $P(z)$ in the middle and low-frequency band.

To determine the gain K_{r}, $H(z)$ is transformed into the frequency domain. By substituting $z = e^{j\omega T_s}$ into $P(z)$ and $S(z)$, we can get

$$\begin{cases} P\left(e^{j\omega T_s}\right) = A_P(\omega)\, e^{j\theta_P(\omega)} \\ S\left(e^{j\omega T_s}\right) = A_S(\omega)\, e^{j\theta_S(\omega)} \end{cases} \tag{47}$$

where $A_{\mathrm{P}}(\omega)$ and $\theta_{\mathrm{P}}(\omega)$ are the amplitude and phase-frequency characteristics of P, respectively. $A_{\mathrm{S}}(\omega)$ and $\theta_{\mathrm{S}}(\omega)$ are the amplitude and phase-frequency characteristics of S, respectively.

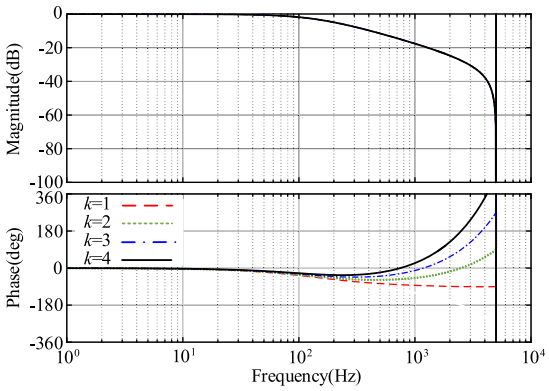

Fig. 11. Bode plot of $z^k P(z)$ with different k.

Substituting (47) into $H(e^{j\omega T_S})$, one can be obtained as

$$|H| = \left| Q - A_P(\omega) A_S(\omega) K_r e^{j\delta(\omega)} \right| < 1 \tag{48}$$

where $\delta(\omega) = \theta_P(\omega) + \theta_S(\omega) + k\omega T_s$. By transforming (48), the stability condition is expressed as

$$Q^2 - 2QA_P(\omega) A_S(\omega) K_r \cos\delta(\omega) + (A_P(\omega) A_S(\omega) K_r)^2 < 1. \tag{49}$$

Therefore, the gain K_r of RC must satisfy

$$0 < K_r < \frac{Q\cos\delta(\omega) + \sqrt{(Q\cos\delta(\omega))^2 - (Q^2-1)}}{A_P(\omega) A_S(\omega)}. \tag{50}$$

To improve the robustness of the controller in case of parameter deviation, the multiplicative deviation term $\triangle(z)$ can be introduced into the equivalent plant $P(z)$

$$P'(z) = P(z)(1 + \Delta(z)). \tag{51}$$

Assuming that the equivalent controlled object $P'(z)$ is stable after the parameter deviation, and $|\triangle(z)| \le \triangle_{\max}$, $\triangle_{\max}$ is the maximum deviation, Φ is the maximum phase deviation, in this case, (50) can be modified and expressed as

$$0 < K_r < \frac{\min\left\{Q\cos\delta(\omega+\phi) + \sqrt{(Q\cos\delta(\omega+\phi))^2 - (Q^2-1)}\right\}}{\max\{A_P(\omega) A_S(\omega)(1+\Delta_{\max})\}}. \tag{52}$$

Using (50), the larger K_r can accelerate the error convergence speed and reduce the steady-state tracking error. Considering that the parameter deviation shown in (52) will reduce the selection range of K_r, and a certain margin is required. Therefore, in this article, $K_r = 0.95$ is selected, and the simulation and experimental control parameters of RC are listed in Table II.

Employing the above-stated design parameters, the Nyquist plot of $H(z)$ can be obtained, as shown in Fig. 12. It can be seen that $H(z)$ is located in the unit circle, which is evidence of the system stability. The amplitude of $H(z)$ is small in the low-frequency range, which guarantees the robust convergence speed and higher steady-state tracking performance.

To investigate the implications of proposed RC-based arm current controller, the frequency characteristics of the disturbances suppression with PI and PI-RC control are shown in Fig. 13. Compared with the curve in the figure, in the case of the PI controller only, it can be seen that the attenuation ability is weak. For instance, the attenuation gain at the second-order harmonic is recorded –3.9 dB only, which indicates the poor ability to restrain the second-order harmonic circulating current. However, the inclusion of the RC control strategy offers strong attenuation ability in the second-order harmonic, i.e., –31.2 dB, it consequently suppresses the harmonic currents.

TABLE II
SIMULATION AND EXPERIMENTAL CONTROL PARAMETERS

Parameters	Simulation Value	Experimental value
N	200	200
$Q(z)$	0.97	0.97
$S(z)$	$0.25z+0.5+0.25z^{-1}$	$0.25z+0.5+0.25z^{-1}$
k	3	3
K_r	1	0.95

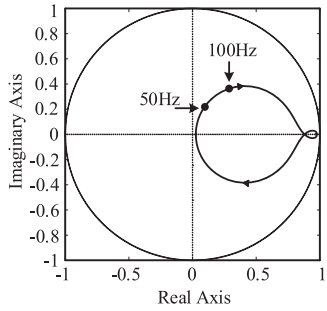

Fig. 12. Nyquist plot of $H(z)$.

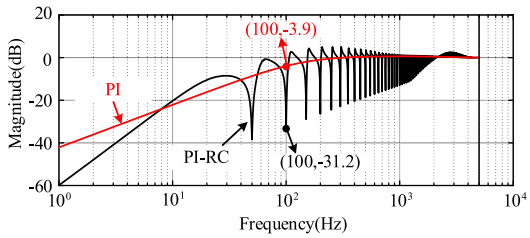

Fig. 13. Harmonic disturbances suppression characteristics of PI control and RC control.

VI. SIMULATION RESULTS

To evaluate the effectiveness and feasibility of the proposed comprehensive control strategy of MMC, three-phase MMC system simulations have carried out in MATLAB/Simulink software using the simulation parameters described in Tables I and II.

A. Simulation Results of Dynamic Response

The dynamic response has been investigated by setting the MMC to operate in the power control mode, and the active power $P_{dc} = 800$ kW (forward) changes to $P_{dc} = -800$ kW (reverse) during a time interval of $t = 4.0$–4.1 s, the corresponding waveforms of voltage and current on the ac-side and dc-side along with the arm current of MMC are shown in Fig. 14. According to Fig. 14(a)–(c), before $t = 4.0$ s, the three-phase

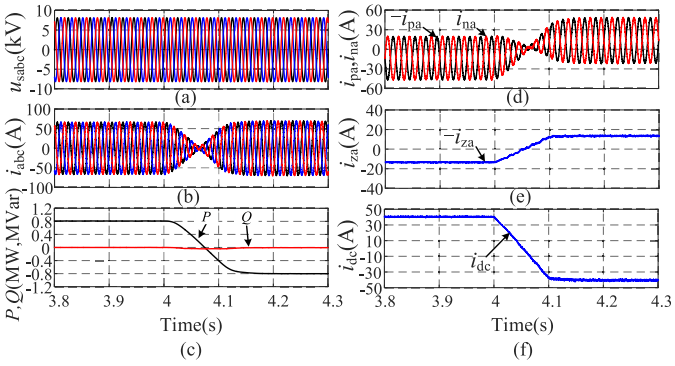

Fig. 14. Voltage and current waveforms of MMC. (a) AC-side voltage. (b) AC-side current. (c) Active and reactive power. (d) A-phase arm current. (e) A-phase circulating current. (f) DC-bus current.

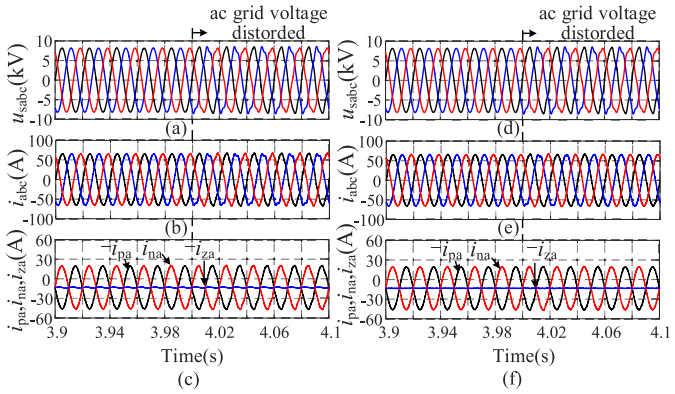

Fig. 15. Simulation results of MMC using the PI control and the proposed control method under the ac grid voltage distortion. (a)–(c) AC-side voltage, ac-side current and arm current with PI control. (d)–(f) AC-side voltage, ac-side current and arm current with proposed improved comprehensive control strategy.

voltage and current of the ac-side are kept in the same phase and the power flow from the ac side to the dc side. After $t = 4.0$–4.1 s, the three-phase voltage and current at the ac-side are reversed. The transmission power always tracks the given value, indicating that the MMC power is controllable. It can be seen in Fig. 14(c) that the transmission power changes smoothly in the process of reversal power flow. Similarly, Fig. 14(d) and (e) reflects that during reversal power flow, the arm current always retains a good sinusoidal waveform, and almost no distortion occurs in the arm current; where the circulating current contains only the dc component and the circulating current with the double-frequency and above can be suppressed.

B. Simulation Results Under Grid Voltage Distortion

In order to verify the control performance of the MMC system under ac-side grid voltage distortion, the ac-side voltage is set at $t = 4.0$ s to generate distortion, including 5 p.u. fifth-order harmonic and 3 p.u. seventh-order harmonic, and other parameters remain unchanged.

The results obtained by the proposed method and the PI controller under the ac grid voltage distortion are shown in Fig. 15. It can be seen from Fig. 15(a)–(c) that when the grid voltage is distorted, the three-phase current at the ac-side and the upper and lower arm currents contain a large number of fifth- and

TABLE III
RESULTS OF SPECTRUM ANALYSIS FOR EACH CURRENT WITH DIFFERENT CONTROL UNDER AC GRID VOLTAGE DISTORTION

Item	i_a			i_{pa}				i_{za}
	THD /%	5th /%	7th /%	THD /%	2nd /%	5th /%	7th /%	2nd /%
PI	4.43	3.41	2.62	5.03	2.30	3.39	2.63	5.69
PI-R_1-R_2	4.45	3.41	2.66	4.55	0.6	3.44	2.61	1.70
Proposed method	1.20	0.15	0.17	1.36	0.09	0.10	0.22	0.08

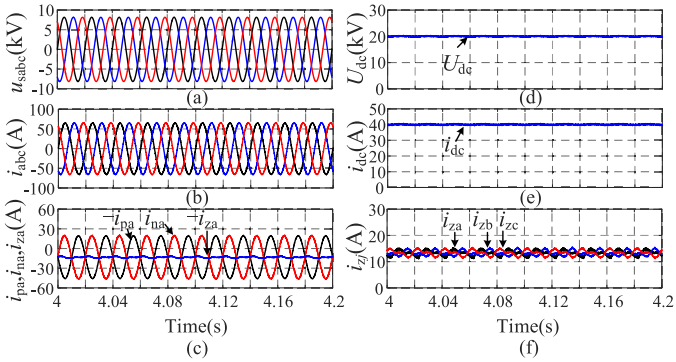

Fig. 16. Simulation results of MMC using the PI control under arm parameter asymmetry. (a) AC-side voltage. (b) AC-side current. (c) A-phase arm current and circulating current. (d) DC-bus voltage. (e) DC-bus current. (f) Three phase circulating currents.

seventh-order harmonic currents, as shown in Fig. 15(b) and (c), which shows that PI control has a weak ability to restrain the grid voltage distortion. The results of the spectrum analysis for each current with different control methods are shown in Table III. When PI control is adopted only, the ac-side current contains 3.41% fifth-order and 2.62% seventh-order harmonic currents, and the upper arm current contains 2.30% second-order, 3.39% fifth-order, and 2.63% seventh-order harmonic currents. The inclusion of multiresonant controllers PI–R_1–R_2 eliminates the low-order harmonics; however, the higher order harmonics are still existing, e.g., fifth and seventh order. The steady-state waveform and the corresponding spectrum by applying the proposed RC-based arm current control are shown in Fig. 15(d)–(f) and Table III. It can be seen that the second-, fifth-, and seventh-order harmonic currents in the ac-side currents and the arm currents are completely eliminated, which demonstrates the merits and strong ability of the proposed control to restrain the grid voltage distortion. Thus, it enables the use of RC-based arm current control to achieve a satisfactory total harmonics distortion (THD) level of the ac-side, dc-side, and arm currents.

C. Simulation Results Under Arm Parameters Asymmetry

To evaluate the control performance of MMC system under arm parameters asymmetry, $L_{pa} = 150\%L_{pa0}$, $R_{pa} = 0\ \Omega$, and $L_{na} = 50\%L_{na0}$, $R_{na} = 0.5\ \Omega$ (subscript "0" indicates the rated value) are set.

The control performances of the MMC with the PI control are displayed in Fig. 16. As shown in Fig. 16(b) and Table IV, a small dc-component in the ac-side current and a small fundamental

TABLE IV
RESULTS OF SPECTRUM ANALYSIS FOR EACH CURRENT WITH DIFFERENT CONTROL UNDER ARM PARAMETERS ASYMMETRY

Item	i_a			i_{pa}		i_{za}		i_{dc}
	THD /%	0Hz /%	2nd /%	THD /%	2nd /%	fund. /%	2nd /%	fund. /%
PI	1.44	0.2	0.48	2.29	2.09	8.83	5.54	0.6
PI-R_1-R_2	1.34	0.02	0.10	1.24	0.81	3.42	1.85	0.54
Proposed method	1.38	0.03	0.13	0.99	0.1	0.98	0.2	0.09

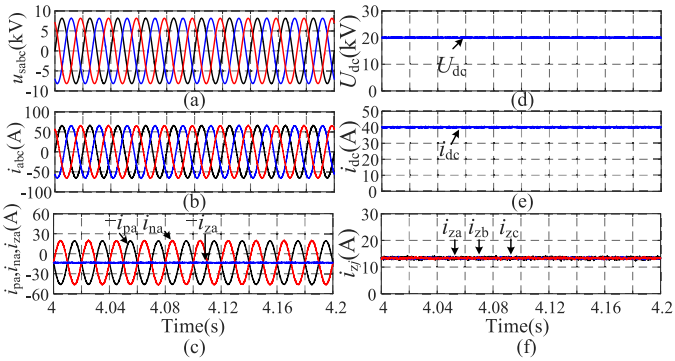

Fig. 17. Simulation results of MMC using the proposed improved comprehensive control method under arm parameters asymmetry. (a) AC-side voltage. (b) AC-side current. (c) A-phase arm current and circulating current. (d) DC-bus voltage. (e) DC-bus current. (f) Three phase circulating currents.

ac-component in the dc-bus current are caused because of the arm parameters asymmetry. Moreover, 5.54% second-order and 8.83% fundamental-frequency circulating currents are recorded in the MMC, as shown in Fig. 16(f) and Table IV, which deteriorates the operation performance and result in higher losses. After the multiresonant controllers R_1 and R_2 are added, the low-order harmonics are eliminated. With the proposed control, it is clearly justified that the dc-component in the ac-side current and the ripples in the dc-bus current are well suppressed, as shown in Fig. 17(b), (e), and Table IV. The circulating currents in each phase are improved, which only contains the dc component only, as shown in Fig. 17(f).

D. Simulation Results Under AC Grid Voltage Asymmetry

To evaluate the control performance of MMC under the three-phase asymmetry fault condition of the ac grid, the a-phase voltage drop of 50% at the ac grid is kept for a time interval, i.e., $t = 3.0$–3.2 s, and 20% of a-phase voltage rise of the ac grid is set at $t = 3.4$ s, whereas 40% of the three-phase voltage drop of the ac power grid is set at $t = 3.8$ s. MMC works in the constant dc-bus voltage control mode.

Fig. 18 shows the results of MMC by employing the DCCI-based leg-averaging control under the ac grid voltage fault condition. The simulation results reflected in Fig. 18(a) show the resultant waveforms of the ac grid voltage under the different fault conditions. In the case of single-phase voltage drop appears, the ac-side current of MMC always preserves three-phase symmetry resulting in eliminating the negative-sequence component, as shown in Fig. 18(b). Moreover, during the fault period of the

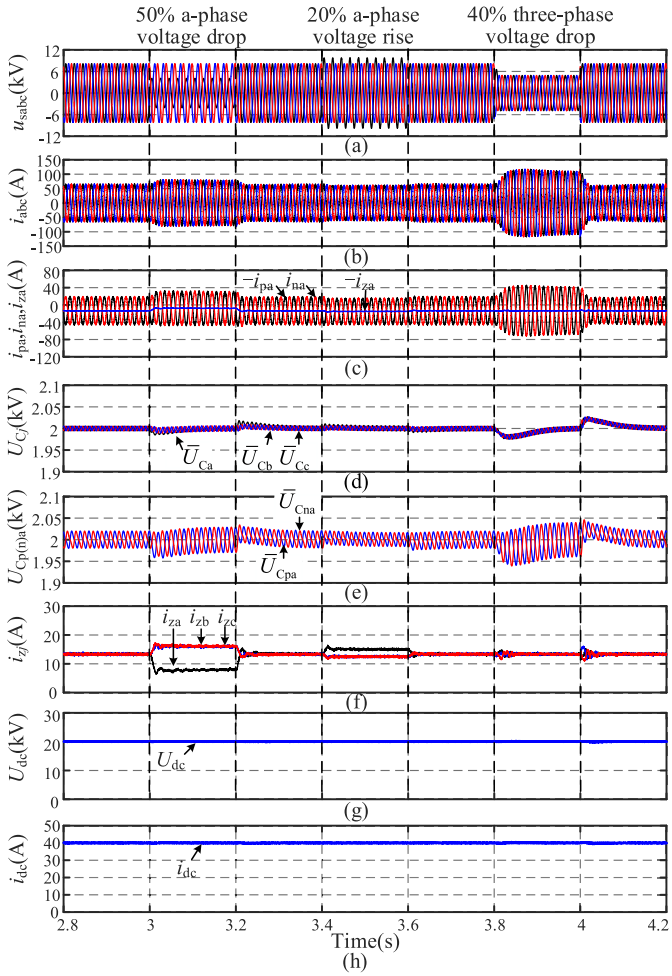

Fig. 18. Simulation results of MMC by employing the DCCI-based leg-averaging control under the ac grid voltage fault. (a) AC-side voltage. (b) AC-side current. (c) A-phase arm current and circulating current. (d) Leg capacitor voltages of three phase. (e) A-phase capacitor voltages of upper and lower arms. (f) Circulating currents. (g) DC-side voltage. (h) DC-side current.

ac power grid, the sinusoidal waveforms of ac-side current and arm current always retain with good quality and eliminate the ac components in the circulating currents. The circulating current only contains the dc component, as shown in Fig. 18(c) and (f). It can be seen from Fig. 18(f) that in the case of voltage asymmetry in the ac power grid, the three-phase dc-circulating current is no longer symmetrical. The output negative-sequence voltage of the arm changes the size of each phase dc circulating current, making the dc-circulating current no longer evenly divided. Fig. 18(d) and (e) shows the obtained results in the case of voltage fault at the ac power grid, where the SM capacitor voltages of three-legs and arms are invariably symmetrical and maintained at 2000 V; besides, Fig. 18(g) and (h) indicates that the voltage and current at dc-bus are not affected, and no low-order ripples appear at the dc side.

Fig. 19 displays MMC findings by using the proposed NSCI leg-averaging control under the ac grid voltage fault. In comparison with the DCCI-based method, when the grid voltage is asymmetrical, the proposed NSCI-based leg averaging control method results in the asymmetry of the ac-side currents in order

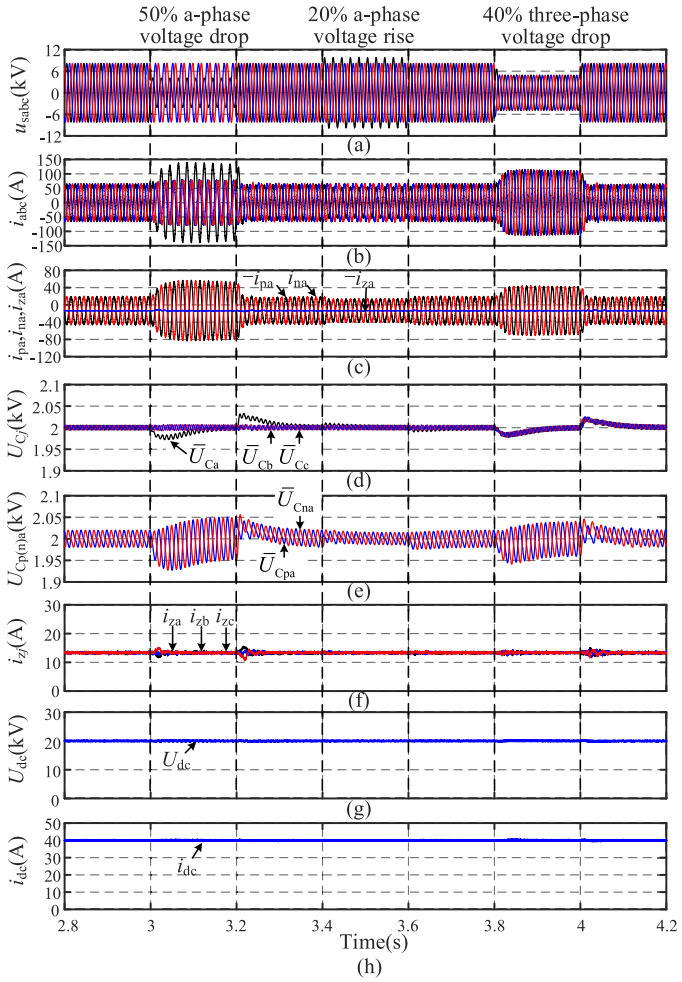

Fig. 19. Simulation results of MMC by employing the NSCI-based leg-averaging control under the ac grid voltage fault. (a) AC-side voltage. (b) AC-side current. (c) A-phase arm current and circulating current. (d) Leg capacitor voltages of three phase. (e) A-phase capacitor voltages of upper and lower arms. (f) Circulating currents. (g) DC-side voltage. (h) DC-side current.

to balance three legs energy, as shown in Fig. 19(b). From Fig. 19(f), it can be seen that the three-phase dc circulating currents are always symmetrical to the NSCI-based method in the case of voltage asymmetry in the ac power grid. Furthermore, Fig. 19(g) and (h) shows that the voltage and current at dc-bus are not affected either.

Moreover, the obtained results by the proposed control method are evaluated via comparing with other existing method reported in [15] under the phasors asymmetry of ac-side grid voltage conditions. It can be argued that the referred control method in [15] may obtain the asymmetrical ac-side currents with three single-phase PLL, as shown in Fig. 20(c). When the phasors of ac-side grid voltage are asymmetrical, the output of three single-phase PLL may contain zero-sequence component and be asymmetrical too. The zero-sequence current canceller will result in the ac-side three-phase reference current asymmetry. On the other hand, despite the amplitude and the phase of ac-side grid voltage are symmetrical or not, the ac-side current consistently sustains in symmetry with the three-phase PS-PLL.

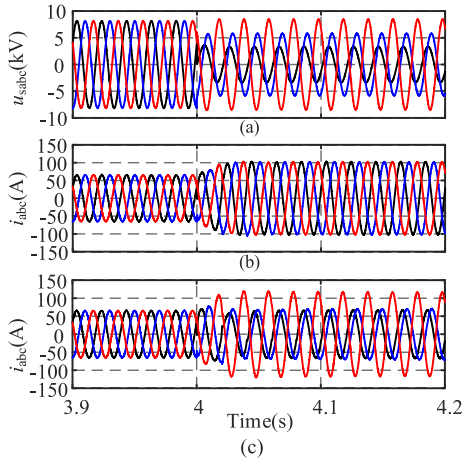

Fig. 20. Simulation results under the amplitude and phase asymmetry of ac grid voltage. (a) AC-side voltage. (b) AC-side current by the proposed control with three-phase PS-PLL. (c) AC-side current by the control method in [15] with three single-phase PLL.

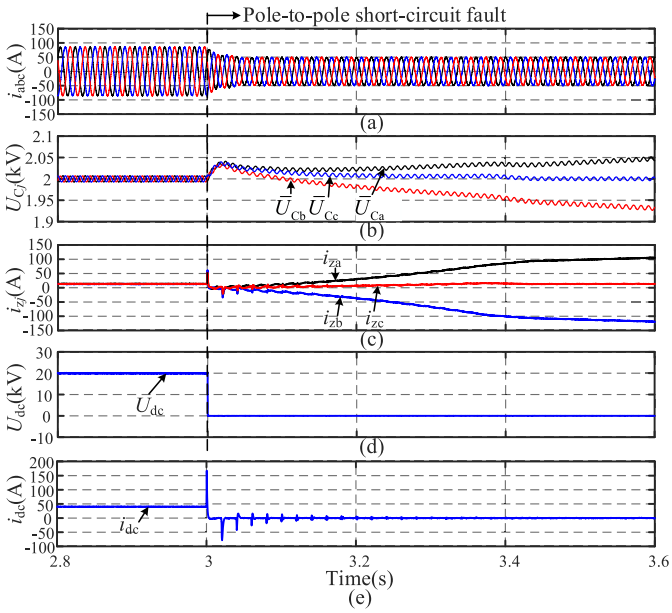

Fig. 21. Simulation results of MMC by employing the DCCI-based leg-averaging control under the pole-to-pole dc short circuit fault. (a) AC-side current. (b) Leg capacitor voltages of three phase. (c) Circulating currents. (d) DC-side voltage. (e) DC-side current.

E. Simulation Results under Pole-to-Pole DC Short-Circuit Fault

Figs. 21 and 22 show the simulation results for full-bridge MMC using the proposed DCCI- and NSCI-based leg-averaging control methods under pole-to-pole dc short-circuit fault condition, respectively. For simplicity of the simulation, the undervoltage detection is used to detect dc fault. Before pole-to-pole dc short-circuit fault occurs at $t = 3.0$ s, the MMC delivers 800 kW active power and 500 kVar reactive power. The parallel parasitic resistances at SMs of three legs are set as 8000, 3000, and 5000 Ω to emulate the unbalanced conditions. It is clearly shown in Fig. 21 that even though the DCCI-based leg-averaging control method kept injecting the dc circulating current, it is unable to

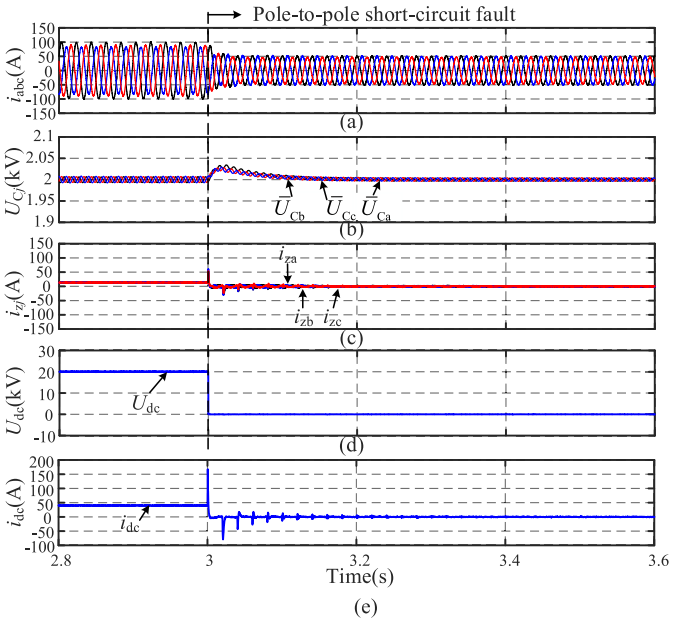

Fig. 22. Simulation results of MMC by employing the NSCI-based leg-averaging control under the pole-to-pole dc short circuit fault. (a) AC-side current. (b) Leg capacitor voltages of three phase. (c) Circulating currents. (d) DC-side voltage. (e) DC-side current.

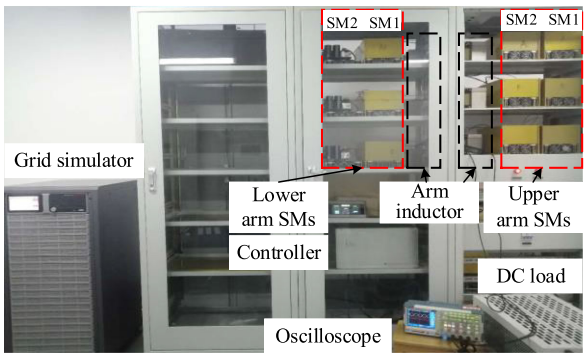

Fig. 23. Photograph of the scaled-down three-phase MMC experimental setup.

force and average three legs voltage to the reference value due to the dc-bus voltage is collapsed to zero during pole-to-pole dc short-circuit fault. In contrast, as shown in Fig. 22 using the proposed NSCI-based control method, the average capacitor voltages of three legs are controlled at the reference value during the pole-to-pole dc short-circuit fault ride-through.

VII. Experimental Results

A three-phase MMC experimental work is carried out to prove the effectiveness of the proposed comprehensive control strategy of MMC and to compare different control methods. The circuit topology of MMC is shown in Fig. 1. Photograph of the scaled-down three-phase MMC experimental setup is shown in Fig. 23. The MMC experimental setup consists of three-phase MMC, controller, dc load, grid, and oscilloscope.

Each arm is formed by a stack of two full-bridge submodules and one arm inductor. The sub-module can be configured as a full-bridge or half-bridge. A single 2 mH dc inductor is used to

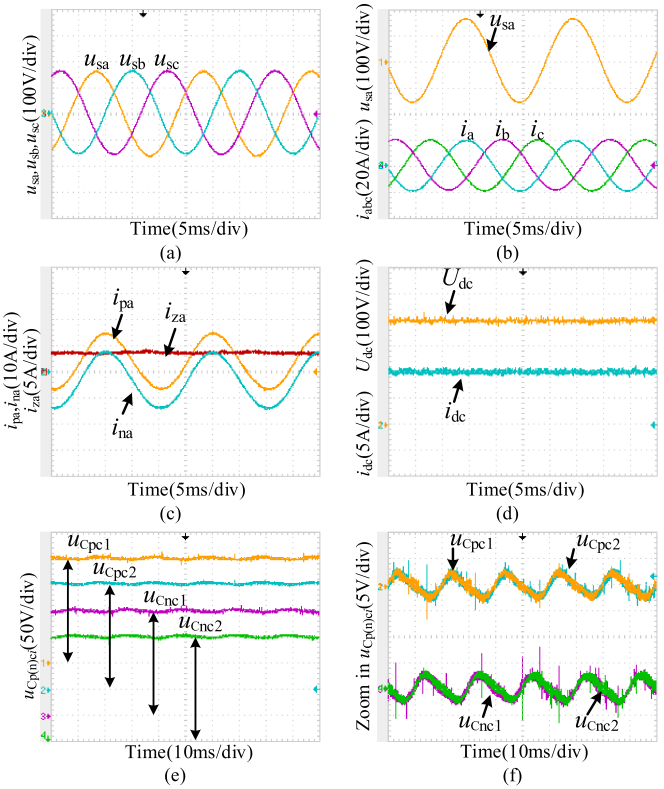

Fig. 24. Experimental results of steady state. (a) AC-side grid voltage. (b) AC-side current. (c) A-phase arm current. (d) DC-side voltage. (e) C-phase capacitor voltages. (f) Zoom in c-phase capacitor voltages.

filter out the switching ripples. The controller is implemented with DSP+FPGA, where DSP is responsible for the control algorithm, and FPGA realizes the modulation. The innerarm submodule individual-balancing control method with CPS-SPWM is adopted. The overall program execution time in the DSP for the proposed control strategy is about 36 μs, which is with lower computational burden than the other advanced methods, such as MPC [43]. The equivalent switching frequencies for simulation and experiment are 20 kHz. The parameters used in the experimental prototype are shown in Table I, and the control parameters are shown in Table II.

A. Experimental Results of Steady State and Dynamic Response Performance

Fig. 24 shows the steady-state experimental results of the MMC system with the proposed control strategy. As shown in Fig. 24(b) and (d), MMC outputs high quality in terms of three-phase sinusoidal currents, dc-bus voltage, and dc-bus current without ripples. The results obtained in the steady-state condition are shown in Fig. 24(c), it can be seen that the arm currents are sinusoidal, and the circulating current contains dc component only, which effectively suppresses the undesired ac-component circulating currents. Fig. 24(e) and (f) represents that the SMs capacitor voltage keeps in its reference value.

The dynamic response of the MMC is shown in Fig. 25 under the dc load step by changing the dc load from 2 to 4 kW; accordingly, the dc-bus current will step from 5 to 10 A. As shown in

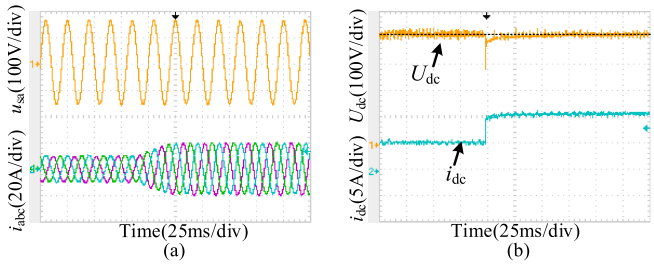

Fig. 25. Experimental results of dynamic response of MMC under dc load step. (a) AC-side voltage and current. (b) DC-side voltage and current.

Fig. 25(b), the dynamic response of the three-phase current at the ac side has accomplished in two fundamental frequency cycles, and the current waveform changes smoothly without distortion during the transition process. It should be noted that the response speed of the outer voltage loop is much slower than that of the inner-current loop, so the dynamic response speed of the dc load step process is mainly determined by the outer-voltage loop.

B. Experimental Results of Multifrequency Harmonics Suppression Performance

The multifrequency harmonics suppression performance has been demonstrated via experiments, where the dead time was set as 5 μs for better visibility of multifrequency harmonics suppression performance. Fig. 26 shows the experimental waveforms of the MMC system employing different control strategies under the dead time $t_d = 5$ μs. Observations in Fig. 26 clearly indicate the presence of a large second- (8.41%), fourth- (4.68%), fifth-, sixth-, seventh-, and eighth-order harmonics in the arm currents when only a PI regulator is applied, and the THD is up to 10.26%. As shown in Fig. 26(a)–(c), the ac-side, dc-side, and arm currents are seriously distorted with PI control. After the multiresonant controllers PI–R_1–R_2 are added, the second-order harmonic is eliminated. However, it can be observed from the fast Fourier transform results of the arm current in Fig. 26(h) that, the dead time also induces higher order harmonics, and the higher orders still exist, e.g., fourth-(6.64%), fifth-(0.61%), sixth-(0.74%), seventh-(1.8%), and eighth-order (0.78%) harmonics. In that case, only incorporating the R_1–R_2 compensators may not achieve a satisfactory THD level (7.83%). In contrast, the results obtained by the proposed RC-based arm current control method, as shown in Fig. 26(i)–(l), affirm the elimination of ac circulating current along with the sinusoidal waveform of arm current, and the THD of arm current is about 3.07%. In short, with the proposed RC-based arm current control method, even-order and odd-order harmonics are eliminated on both the ac-side, dc-side, and circulating currents, thus improving the voltage and current quality even under large disturbances.

C. Experimental Results Under AC Grid Fault

The control performances under ac grid fault with 50% voltage drop of single-phase, two-phase, and three-phase are investigated. The experimental waveforms of the MMC system are shown in Figs. 27 and 28. It can be seen from Figs. 27(a) and (c) and 28(b) and (d) that both PI-control and proposed control can achieve symmetrical control of ac-side current with DCCI-based leg-averaging control in case of asymmetrical or symmetrical grid voltage. According to the conservation of ac and dc power, when the ac voltage asymmetry is more serious, the amplitude of ac-side current will be large. However, with PI control, the arm current is distorted, and the unwanted ac-component harmonics exist in the circulating current, as shown in Fig. 27(b), which increases the amplitude of arm current and the power loss. It is pertinent to mention that the proposed control method is capable of retaining the sinusoidal arm current under the grid voltage asymmetry condition and eliminate the ac circulating currents. Comparing the circulating current in Figs. 27(b) and (d) and 24(c), it can be observed that due to the existence of negative- and zero-sequence voltages, the three-phase circulating current will no longer be symmetrical, which is consistent with the theoretical analysis in Section II.

Fig. 29 demonstrates the experimental results of the proposed NSCI-based leg-averaging control with the normal and a 50% single-phase voltage drop operations. The three-phase submodule capacitor voltages were regulated at its reference value with the proposed NSCI-based leg-averaging control, as shown in Fig. 29(a) and (c). It is clearly shown in Fig. 29(b) that the proposed NSCI-based leg-averaging control can achieve symmetrical control of ac-side current in case of normal operation. In the case of the asymmetrical grid voltage, compared with the DCCI method, the proposed NSCI leg-averaging control method results in ac-side current asymmetry so that three-leg energy is balanced, as shown in 29(d).

Since the magnitude of the negative-sequence current injected is very small and disappears under normal operating conditions [as shown in Fig. 29(b)], it can be considered as a promising solution for both the ac fault ride through and the dc fault ride through.

Fig. 30 shows the experimental result of three-phase capacitor voltages with and without employing the proposed NSCI-based leg-averaging control under 10% a-phase grid voltage drop. The three-phase submodule capacitor voltages are regulated at its reference value with proposed NSCI-based leg-averaging control. In contrast, the three-phase submodule capacitor voltages will gradually diverge after disabling the NSCI-based leg-averaging control, which may even threaten the safety of the device.

D. Experimental Results Under AC and DC Grid Fault

To demonstrate the complex ac and dc FRT capability of the proposed leg-averaging control method for MMC, the 50% ac voltage drop is emulated to create unbalanced ac grid conditions, and the dc-bus pole-to-pole short circuit fault is emulated by controlling the dc-bus voltage from nominal value 400 to 0 V.

Fig. 31 shows the experimental results of MMC under both 50% a-phase ac voltage drop and dc-bus pole-to-pole voltage collapsed to zero with the NSCI-based leg-averaging control. It can be observed that only a negative-sequence current injection is used to balance the legs power flow during the ac and dc FRT period. As shown in Fig. 31(a), the SM capacitor voltages of three legs are well balanced and maintained at its reference value 200 V. In addition, the MMC is able to continuously deliver the

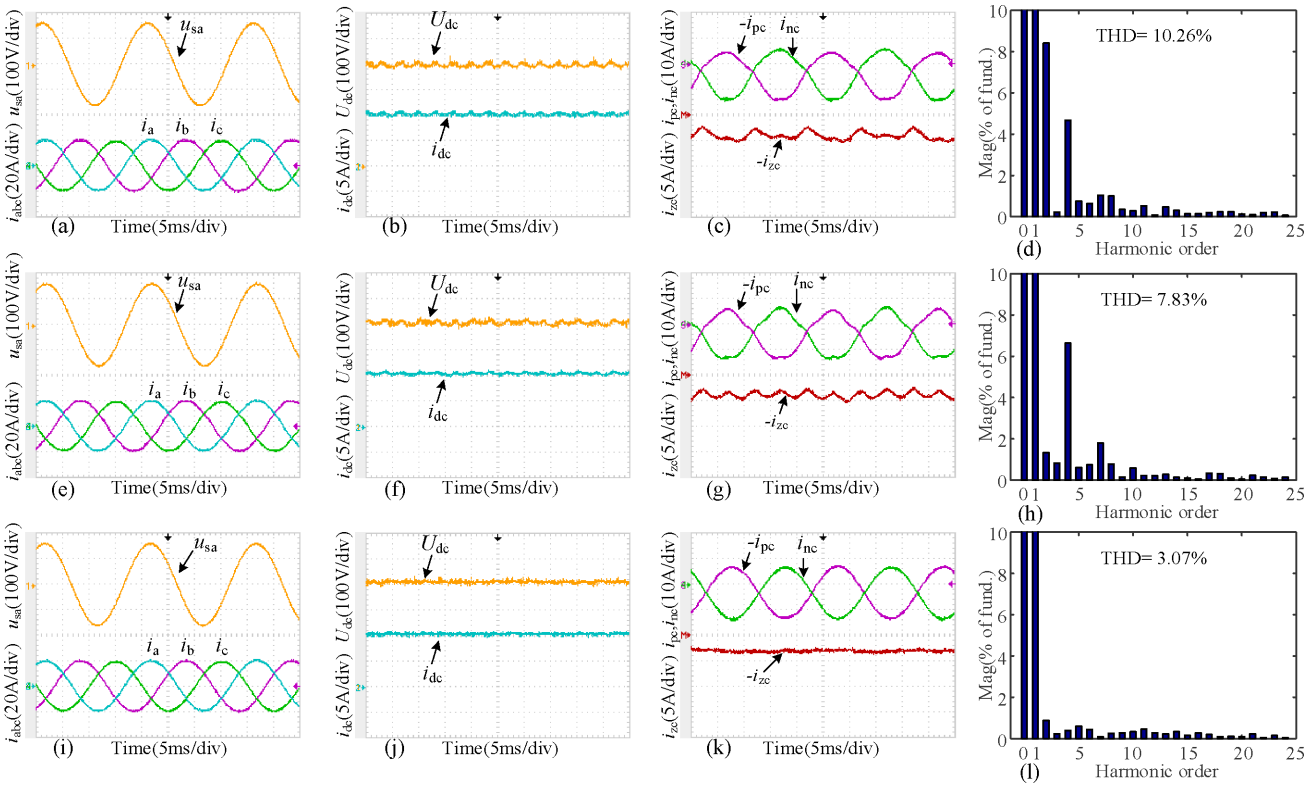

Fig. 26. Experimental results of MMC ac-side voltage and current, dc-side voltage and current, arm current and harmonic spectrum of arm current with different control strategies under dead time $t_d = 5\ \mu s$. (a)–(d) PI control. (e)–(h) PI–R_1–R_2 control. (i)–(l) Proposed RC-based arm current control.

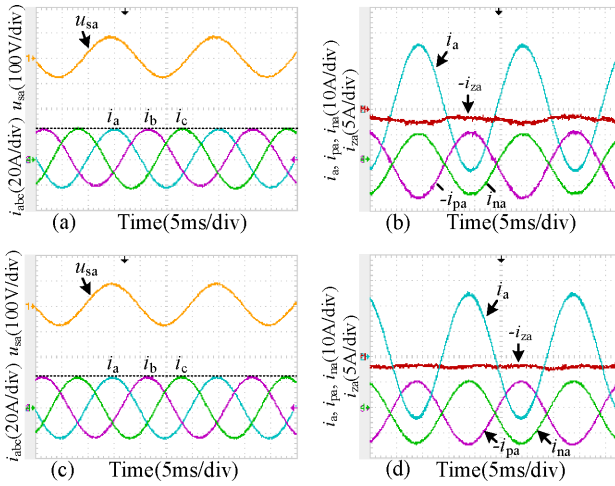

Fig. 27. Experimental results of MMC with different control strategies under 50% single-phase voltage drop. (a), (b) AC-side voltage, ac-side current, and arm current with PI control. (c), (d) AC-side voltage, ac-side current, and arm current with proposed control in this article.

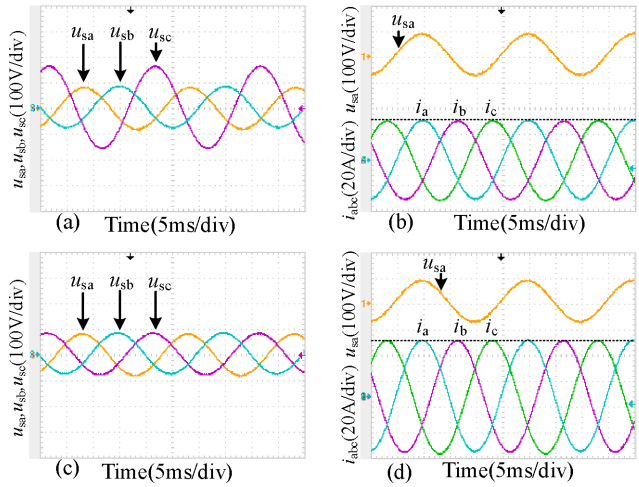

Fig. 28. Experimental results of MMC with DCCI-based leg-averaging control. (a) 50% two-phase voltage drop. (b) AC-side voltage and current. (c) 50% three-phase voltage drop. (d) AC-side voltage and current.

reactive power (about 1.65 kVar) to the ac grid under both the ac and dc FRT period, as shown in Fig. 31(b). However, as shown in Fig. 31(b), in order to perform the leg-averaging control, it is necessary to inject a high negative-sequence current into the ac grid under the asymmetry ac grid fault, and the maximum ac-side current is up to 26 A, consequently increasing the IGBT current stress, the converter power losses, and the ripple in the capacitor voltage.

Fig. 32 shows the experimental results of MMC under 50% a-phase ac voltage drop, and dc-bus pole-to-pole voltage collapsed to zero with the proposed leg-averaging control method by seamlessly switching DCCI to NSCI. During the ac grid FRT period, the ac-side currents are symmetrical with DCCI, i.e., $I^- = 0$ and shown in Fig. 32(b). When $K = 1$, only a small dc-circulating current is injected to balance the leg-capacitor voltage under the ac grid fault. However, as discussed in Section II, it should be emphasized that the DCCI-based leg-averaging control scheme

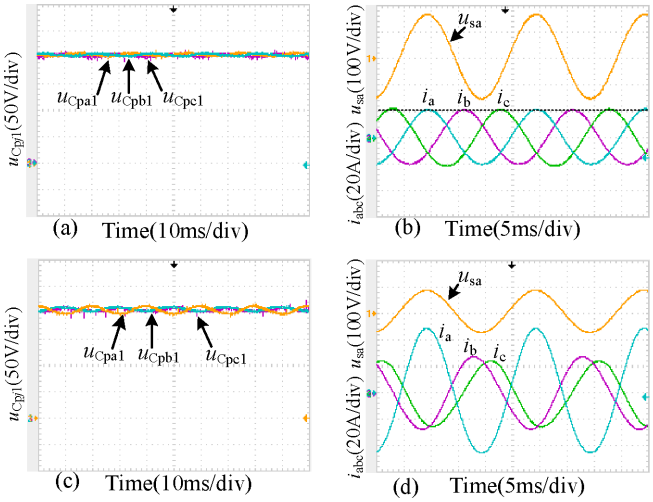

Fig. 29. Experimental results of MMC with proposed NSCI-based leg-averaging control. (a) Three-phase capacitor voltages of submodule #1 under normal operation. (b) AC-side voltage and current under normal operation. (c) Three-phase capacitor voltages of submodule #1 under asymmetrical operation with 50% single-phase voltage drop. (d) AC-side voltage and current under asymmetrical operation with 50% single-phase voltage drop.

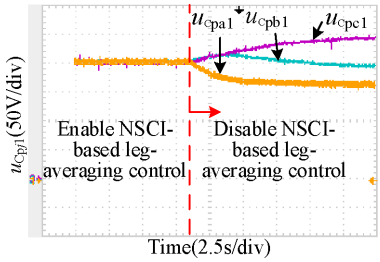

Fig. 30. Experimental results of MMC with and without employing the proposed NSCI-based leg-averaging control.

would be invalid when the dc-bus voltage collapses to zero during the dc grid fault. Therefore, the DCCI has to actively change to NSCI during dc-bus voltage collapsed to zero. Thanks to the proposed control, the ac-side currents can be symmetrical during the ac grid FRT, and the MMC is able to continuously deliver the reactive power (about 1.65 kVar) to the ac grid under both the ac and dc FRT period. Compared to the NSCI method in Fig. 31, the maximum ac-side current is decreased to 16 A.

In summary, the dc-circulating current and negative-sequence current component can be flexibly combined, which improves control DOFs for leg-averaging control. Therefore, it is recommended that the weight factor in (37) should be set $K = 1$ (DCCI) if the dc-bus voltage is stable, thus reducing both the power losses and current stress, also preventing that the ac-side imbalances affect the dc-side. The DCCI must seamlessly change to NSCI to realize the dc FRT when the dc-bus voltage collapses to zero, providing reactive power compensation to the ac grid continuously and ensuring uninterrupted controllability of the MMC stations at all times.

Based on the abovementioned experimental results and analysis, various important factors such as grid voltage distortion and asymmetry, dc-bus short-circuit fault, arm parameters asymmetry, and dead time seriously affect the performance of the

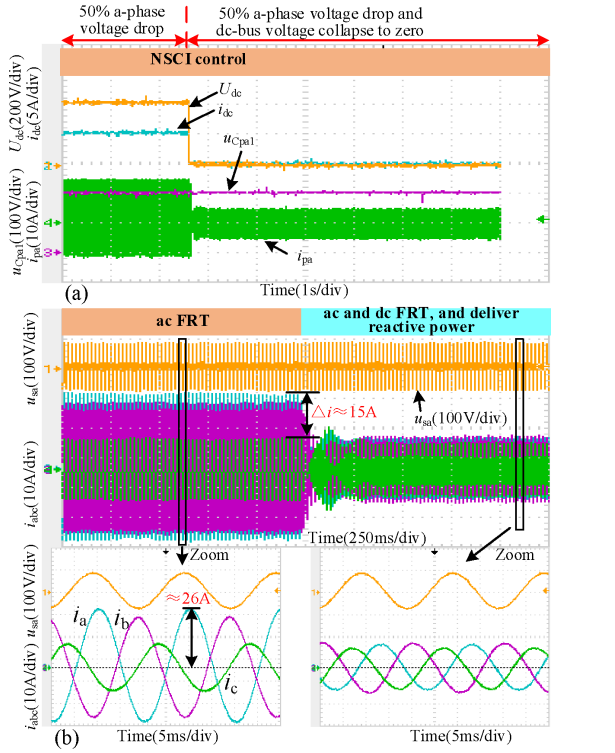

Fig. 31. Experimental results of MMC with employing the NSCI-based leg-averaging control under ac and dc grid fault conditions. (a) DC-bus voltage and current, arm current, and SM capacitor voltage. (b) AC-side three-phase currents.

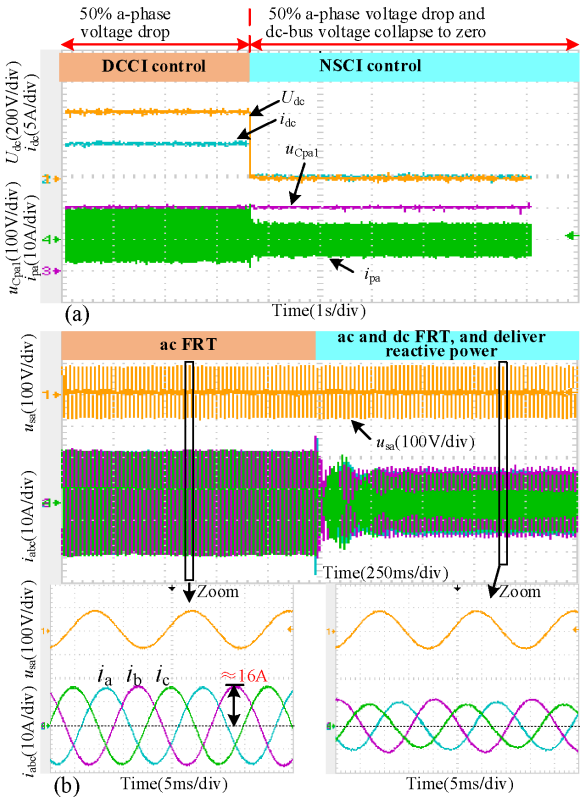

Fig. 32. Experimental results of MMC with employing the DCCI seamlessly switching to the NSCI-based leg-averaging control under the ac and dc grid fault conditions. (a) DC-bus voltage and current, arm current, and SM capacitor voltage. (b) AC-side three-phase currents.

MMC system. The proposed improved comprehensive control strategy for MMC, in this article, can well adapt to all the abovementioned operating conditions and ensure the high quality of voltage and current at both ac-side and dc-side of MMC. Eventually, it improves the operation reliability of the MMC system.

VIII. Conclusion

This article introduces an improved comprehensive control architecture of MMC to realize ac and dc grid fault ride-through and to eliminate harmonics in ac-side and circulating currents under various operating conditions. The proposed comprehensive control architecture consists of improved hierarchical voltage control and repetitive controller-based arm current control. The improved hierarchical voltage control realizes dc-bus voltage/power control, leg-averaging control, arm-balancing control, and individual-balancing control. The DCCI-based leg-averaging control can retain the ac-side current symmetry under asymmetrical conditions. The NSCI-based leg-averaging control is valid, and is viewed as a promising solution both for the ac and the dc fault ride-through. Moreover, these two kinds of control options can be further integrated together seamlessly by switching operation during the ac and dc grid faults. The proposed RC-based arm current control can recognize the control of multifrequency components of arm currents. The proposed comprehensive control strategy can control the MMC without decomposing the positive-, negative-, and zero-sequence of ac-side currents and arm currents. Besides, the proposed strategy does not involve any separate circulating current controller design. The simulation and experimental results verify that the proposed control strategy for MMC, in this article, can well adapt to all the operating conditions such as grid voltage distortion, voltage asymmetry, dc short-circuit fault, arm parameters asymmetry, and dead time, it also ensures the high quality of voltage and current at both ac-side and dc-side of MMC.

References

[1] R. Marquardt, "Modular multilevel converter: an universal concept for HVDC-Networks and extended DC-Bus-applications," in *Proc. Int. Power Electron. Conf.-ECCE ASIA*, 2010, pp. 502–507.

[2] M. A. Perez, S. Bernet, J. Rodriguez, S. Kouro, and R. Lizana, "Circuit topologies, modeling, control schemes, and applications of modular multilevel converters," *IEEE Trans. Power Electron.*, vol. 30, no. 1, pp. 4–17, Jan. 2015.

[3] T. Lüth, M. M. C. Merlin, T. C. Green, F. Hassan, and C. D. Barker, "High-frequency operation of a DC/AC/DC system for HVDC applications," *IEEE Trans. Power Electron.*, vol. 29, no. 8, pp. 4107–4115, Aug. 2014.

[4] Y. Li *et al.*, "A modular multilevel converter type solid state transformer with internal model control method," *Int. J. Electr. Power Energy Syst.*, vol. 85, pp. 153–163, 2017.

[5] M. Saeedifard and R. Iravani, "Dynamic performance of a modular multilevel back-to-back HVDC system," *IEEE Trans. Power Del.*, vol. 25, no. 4, pp. 2903–2912, Oct. 2010.

[6] Q. Tu, Z. Xu, and L. Xu, "Reduced switching-frequency modulation and circulating current suppression for modular multilevel converters," *IEEE Trans. Power Del.*, vol. 26, no. 3, pp. 2009–2017, Jul. 2011.

[7] Z. Liu, S. Miao, Z. Fan, K. Chao, and Y. Liu, "Characteristics analysis and improved arm control of modular multilevel converter under asymmetric operation conditions," *Int. J. Electr. Power Energy Syst.*, vol. 105, pp. 272–282, 2019.

[8] Y. Zhou, D. Jiang, J. Guo, P. Hu, and Y. Liang, "Analysis and control of modular multilevel converters under unbalanced conditions," *IEEE Trans. Power Del.*, vol. 28, no. 4, pp. 1986–1995, Oct. 2013.

[9] R. Zeng, L. Xu, L. Yao, and S. J. Finney, "Analysis and control of modular multilevel converters under asymmetric arm impedance conditions," *IEEE Trans. Ind. Electron.*, vol. 63, no. 1, pp. 71–81, Jan. 2016.

[10] D. Samajdar, T. Bhattacharya, and S. Dey, "A reduced switching frequency sorting algorithm for modular multilevel converter with circulating current suppression feature," *IEEE Trans. Power Electron.*, vol. 34, no. 11, pp. 10480–10491, Nov. 2019.

[11] G. Wang, C. Sun, R. Liu, F. Rong, and F. Li, "Modular multilevel converter control strategy based on arm current control," *Proc. CSEE*, vol. 35, no. 2, pp. 458–464, 2015.

[12] B. S. Riar, T. Geyer, and U. K. Madawala, "Model predictive direct current control of modular multilevel converters: Modeling, analysis, and experimental evaluation," *IEEE Trans. Power Electron.*, vol. 30, no. 1, pp. 431–439, Jan. 2015.

[13] J. Moon, J. Park, D. Kang, and J. Kim, "A control method of HVDC-modular multilevel converter based on arm current under the unbalanced voltage condition," *IEEE Trans. Power Del.*, vol. 30, no. 2, pp. 529–536, Apr. 2015.

[14] Y. Liang, J. Liu, T. Zhang, and Q. Yang, "Arm current control strategy for MMC-HVDC under unbalanced conditions," *IEEE Trans. Power Del.*, vol. 32, no. 1, pp. 125–134, Feb. 2017.

[15] Z. Ou, G. Wang, and L. Zhang, "Modular multilevel converter control strategy based on arm current control under unbalanced grid condition," *IEEE Trans. Power Electron.*, vol. 33, no. 5, pp. 3826–3836, May 2018.

[16] E. Shahriari, F. Gruson, P. Vermeersch, P. Delarue, F. Colas, and X. Guillaud, "A Novel DC fault ride through control methodology for hybrid modular multilevel converters in HVDC systems," *IEEE Trans. Power Del.*, vol. 35, no. 6, pp. 2831–2840, Dec. 2020.

[17] E. Kontos, G. Tsolaridis, R. Teodorescu, and P. Bauer, "Full-bridge MMC DC fault ride-through and STATCOM operation in multi-terminal HVDC grids," *Bull. Pol. Acad. Sci.-Tech. Sci.*, vol. 65, pp. 653–662, 2017.

[18] W. Xiang, W. Lin, L. Xu, and J. Wen, "Enhanced independent pole control of hybrid MMC-HVdc system," *IEEE Trans. Power Del.*, vol. 33, no. 2, pp. 861–872, Apr. 2018.

[19] J. Hu, K. Xu, L. Lin, and R. Zeng, "Analysis and enhanced control of hybrid-MMC-based HVDC systems during asymmetrical DC voltage faults," *IEEE Trans. Power Del.*, vol. 32, no. 3, pp. 1394–1403, Jun. 2017.

[20] S. Cui and S. Sul, "A Comprehensive DC short-circuit fault ride through strategy of hybrid modular multilevel converters (MMCs) for overhead line transmission," *IEEE Trans. Power Electron.*, vol. 31, no. 11, pp. 7780–7796, Nov. 2016.

[21] M. Guan and Z. Xu, "Modeling and control of a modular multilevel converter-based HVDC system under unbalanced grid conditions," *IEEE Trans. Power Electron.*, vol. 27, no. 12, pp. 4858–4867, Dec. 2012.

[22] M. Chai, N. B. Y. Gorla, and S. K. Panda, "Fault detection and localization for cascaded H-Bridge multilevel converter with model predictive control," *IEEE Trans. Power Electron.*, vol. 35, no. 10, pp. 10109–10120, Oct. 2020.

[23] N. B. Y. Gorla, S. Kolluri, M. Chai, and S. K. Panda, "A novel open-circuit fault detection and localization scheme for cascaded h-bridge stage of a three-stage solid state transformer," *IEEE Trans. Power Electron.*, to be published.

[24] S. Yang, Y. Tang, and P. Wang, "Distributed control for a modular *multilevel* converter," *IEEE Trans. Power Electron.*, vol. 33, no. 7, pp. 5578–5591, Jul. 2018.

[25] M. Zhang, L. Huang, W. Yao and Z. Lu, "Circulating harmonic current elimination of a CPS-PWM-based modular multilevel converter with a plug-in repetitive controller," *IEEE Trans. Power Electron.*, vol. 29, no. 4, pp. 2083–2097, Apr. 2014.

[26] W. Jiang, W. Ma, J. Wang, L. Wang, and Y. Gao, "Deadbeat control based on current predictive calibration for grid-connected converter under unbalanced grid voltage," *IEEE Trans. Ind. Electron.*, vol. 64, no. 7, pp. 5479–5491, Jul. 2017.

[27] A. Dekka, B. Wu, V. Yaramasu, R. L. Fuentes, and N. R. Zargari, "Model predictive control of high-power modular multilevel converters—An overview," *IEEE J. Emerg. Sel. Topics Power Electron.*, vol. 7, no. 1, pp. 168–183, Mar. 2019.

[28] M. Jeong, S. Fuchs, and J. Biela, "High performance LQR control of modular multilevel converters with simple control structure and implementation," in *Proc. 22nd Eur. Conf. Power Electron. Appl.*, 2020, pp. P.1–P.10.

[29] R. Guruambeth and R. Ramabadran, "Fuzzy logic controller for partial shaded photovoltaic array fed modular multilevel converter," *IET Power Electron*., vol. 9, no. 8, pp. 1694–1702, Jun. 2016.

[30] S. Yang, P. Wang, and Y. Tang, "Feedback linearization-based current control strategy for modular multilevel converters," *IEEE Trans. Power Electron.*, vol. 33, no. 1, pp. 161–174, Jan. 2018.
[31] S. Kolluri, N. B. Y. Gorla, R. Sapkota, and S. K. Panda, "A new control architecture with spatial comb filter and spatial repetitive controller for circulating current harmonics elimination in a droop-regulated modular multilevel converter for wind farm application," *IEEE Trans. Power Electron.*, vol. 34, no. 11, pp. 10509–10523, Nov. 2019.
[32] S. Madichetty, A. Dasgupta, S. Mishra, C. K. Panigrahi, and G. Basha, "Application of an advanced repetitive controller to mitigate harmonics in MMC with APOD scheme," *IEEE Trans. Power Electron.*, vol. 31, no. 9, pp. 6112–6121, Sep. 2016.
[33] S. Kolluri, N. B. Y. Gorla, and S. K. Panda, "Capacitor voltage ripple suppression in a modular multilevel converter using frequency adaptive spatial repetitive based circulating current controller," *IEEE Trans. Power Electron.*, vol. 35, no. 9, pp. 9839–9849, Sep. 2020.
[34] L. He, K. Zhang, J. Xiong, and S. Fan, "A repetitive control scheme for harmonic suppression of circulating current in modular multilevel converters," *IEEE Trans. Power Electron.*, vol. 30, no. 1, pp. 471–481, Jan. 2015.
[35] S. Yang, P. Wang, Y. Tang, M. Zagrodnik, X. Hu, and K. J. Tseng, "Circulating current suppression in modular multilevel converters with even-harmonic repetitive control," *IEEE Trans. Ind. Appl.*, vol. 54, no. 1, pp. 298–309, Jan./Feb. 2018.
[36] M. Moranchel, I. Sanz, E. J. Bueno, F. Huerta, and F. J. Rodriguez, "Circulating current elimination in modular multilevel converter with repetitive controllers," in *Proc. 42nd Annu. Conf. IEEE Ind. Electron. Soc.*, 2016, pp. 6476–6481.
[37] B. Chen, Y. Chen, C. Tian, J. Yuan, and X. Yao, "Analysis and suppression of circulating harmonic currents in a modular multilevel converter considering the impact of dead time," *IEEE Trans. Power Electron.*, vol. 30, no. 7, pp. 3542–3552, Jul. 2015.
[38] H. Rao *et al.*, "Design aspects of the hybrid HVDC system," *CSEE J. Power Energy Syst.*, 2020.
[39] M. M. C. Merlin *et al.*, "The alternate arm converter: A new hybrid multilevel converter with DC-fault blocking capability," *IEEE Trans. Power Del.*, vol. 29, no. 1, pp. 310–317, Feb. 2014.
[40] G. Tang, Z. Xu, and Y. Zhou, "Impacts of three MMC-HVDC configurations on AC system stability under DC line faults," *IEEE Trans. Power Syst.*, vol. 29, no. 6, pp. 3030–3040, Nov. 2014.
[41] A. E. Leon and S. J. Amodeo, "Energy balancing improvement of modular multilevel converters under unbalanced grid conditions," *IEEE Trans. Power Electron.*, vol. 32, no. 8, pp. 6628–6637, Aug. 2017.
[42] M. Hagiwara, R. Maeda, and H. Akagi, "Control and analysis of the modular multilevel cascade converter based on double-star chopper-cells (MMCC-DSCC)," *IEEE Trans. Power Electron.*, vol. 26, no. 6, pp. 1649–1658, Jun. 2011.
[43] Z. Gong, X. Wu, P. Dai, and R. Zhu, "Modulated model predictive control for MMC-based active front-end rectifiers under unbalanced grid conditions," *IEEE Trans. Ind. Electron.*, vol. 66, no. 3, pp. 2398–2409, Mar. 2019.

Jinmu Lai (Member, IEEE) received the B.S. and M.S. degree in electrical engineering, and the Ph.D. degree from the Huazhong University of Science and Technology, Wuhan, China, in 2014, 2017, and 2020, respectively.

He is currently a Lecturer with the School of Electrical Engineering, Zhengzhou University. His research interests include electric energy router, power quality control, and the application of power electronics in power systems.

Xianggen Yin (Member, IEEE) received the B.S., M.S., and Ph.D. degrees in electrical engineering from the Huazhong University of Science and Technology (HUST), Wuhan, China, in 1982, 1985, and 1989, respectively.

He is currently a Professor with the School of Electrical and Electronic Engineering, HUST. His research interests include protective relaying, power system stability control, and power electronics.

Xin Yin (Member, IEEE) received the B.Eng. degree in electronic engineering from the University of Sheffield, Sheffield, U.K., in 2008, the M.Sc. degree in telecommunication from University College London, London, U.K., in 2009, and the Ph.D. degree in electrical and electronic engineering from the University of Manchester, Manchester, U.K., in 2016.

He is currently a Postdoctoral Research Associate of electrical engineering with the University of Liverpool. His current research interests include control of microgrid with renewable energy and demand-side response.

Zia Ullah (Member, IEEE) received the Ph.D. degree in electrical engineering from the Huazhong University of Science and Technology (HUST), Wuhan, China, in 2020.

He is currently a Postdoctoral Research Fellow with the State Key Laboratory of Advanced Electromagnetic Engineering and Technology, HUST. His research interests include power system optimization, intelligent power distribution system, distribution system planning with RES, operation and control, and power electronics technologies.

Lin Jiang (Member, IEEE) received the B.S. and M.S. degrees from the Huazhong University of Science and Technology, Wuhan, China, in 1992 and 1996, respectively, and the Ph.D. degree from the University of Liverpool, Liverpool, U.K., in 2001, all in electrical engineering.

He is currently a Reader of electrical engineering with the University of Liverpool. His current research interests include control and analysis of power system, smartgrid, and renewable energy.

Zhen Wang received the B.S. degree from the College of Electrical and Information Engineering, North China Electric Power University (Baoding), Baoding, China, in 2016. She is currently working toward the Ph.D. degree with the Huazhong University of Science and Technology, Wuhan, China.

Her current research interests include power electronic and its application to power systems.